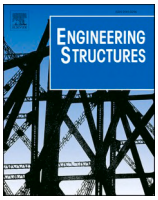
Engineering Structures 274 (2023) 115140



Contents lists available at ScienceDirect

Engineering Structures

journal homepage: www.elsevier.com/locate/engstruct





Behavior of high-performance concrete beams having tension lap spliced anchor-ended bars under repeated loading

Tarek Fawzy [a], Abdel-Hakim Khalil [a], Ahmed Atta [a], Hamdy M. Afefy [a,b], Mohamed Ellithy [a,*]

[a] Department of Structural Engineering, Faculty of Engineering, Tanta University, Tanta, Egypt
[b] Construction Engineering and Management Department, Faculty of Engineering, Pharos University, Alexandria, Egypt

ARTICLE INFO

Keywords:
Lap splice
High-performance concrete
Direct tension
Anchored bars
Plate-ended bars

ABSTRACT

In the current paper, a newly developed technique in tension lap splices of steel bars is presented and investigated to verify its efficiency. Consequently, an experimental and numerical study on sixteen high-performance concrete (HPC) specimens containing lap splices without confining reinforcement were performed. The experimental program comprised two phases; the first one was a preliminary study that involved concrete prisms containing the developed splices and tested under axial tension, while the second phase was four-point flexural testing of RC beams having the adopted tension splices and subjected to repeated loading. Both phases included two sub-groups; a reference sub-group having conventional straight-ended splices and the other sub-group implicated in the newly developed technique based on anchor-ended splices. Experimental tests showed that by applying the developed technique, not only higher tensile stress at failure was achieved but also a bond-induced failure was switched to a flexural failure. Furthermore, a splice length of five times bar diameter was found to be sufficient to achieve the full tensile strength of the reinforcing steel bars in the case of the anchor-ended technique. Finally, numerical modeling was employed to study further parameters about the anchor-ended splices. As a result, a proposed equation was obtained based on statistical analysis to predict the ultimate strength of the anchor-ended splice.

1. Introduction

Bond characteristic between steel reinforcing bars and concrete is one of the most governing factors that control the overall structural performance of reinforced concrete elements. Due to the limited lengths of the manufactured reinforcing steel bars, the reinforcement cannot be extended within the full length of the structural elements in some applications. Connecting these reinforcing bars through concrete can be performed using several patterns. Lap splices, mechanical splices, welded splices, and using anchors (e.g. hooks and headed bars) are several forms of this linking. Subsequently, the development length of reinforcing steel bars with different linking patterns has to be clearly understood. An extensive outline of the previous research work exposes the main governing parameters affecting the splicing behavior; concrete type/strength, concrete cover/bar spacing, confinement condition of the spliced/developed bars, and the techniques used for splicing of bars.

Using various types of concrete affects its compressive/tensile properties and this effect is extended to the bond characteristics. For normal compressive strength of concrete ($f_c' \leq 55$ MPa), the developed bond strength is directly proportional to the square root of the compressive strength of concrete, as reported by many researchers [1–5]. However, for high-strength concrete ($f_c' > 55$ MPa), the average bond strength at failure turns out to be more proportional to the fourth power root of the compressive strength of concrete. As splice length increases in high-strength concrete, the previous relationship may have changed due to the effect of the non-uniform bond stress distribution within the splice length [6,7].

The mechanical properties of concrete are usually affected by adding fibers and this effect is mostly governed by the content and type of fibers. Adding Polypropylene fibers with a volume fraction less than 0.50 % to concrete can slightly decrease its workability but, on the other hand, its resistance to dry shrinkage increases in addition to enhancement of durability [8,9]. For high-performance fiber reinforced concrete, to increase the resistance of dry shrinkage in balance with proper workability, the low content of the polypropylene fibers ranges between 0.25 % and 0.50 % can be considered as the optimum volumetric ratio [10]. For fiber-reinforced cement composites with higher toughness and tensile strength, other types of fibers (polyethylene and steel fibers) are

* Corresponding author at: Department of Structural Engineering, Faculty of Engineering, Tanta University, Egypt.
E-mail address: Mohamed.ezat@f-eng.tanta.edu.eg (M. Ellithy).

https://doi.org/10.1016/j.engstruct.2022.115140
Received 4 April 2021; Received in revised form 17 September 2022; Accepted 12 October 2022
Available online 22 October 2022
0141-0296/© 2022 Elsevier Ltd. All rights reserved.

added with high volumetric ratios up to 4 %. The fibers-induced bridging effect after cracking of these cement composites can effectively limit splitting crack width, enhance the post-cracking tensile capacity of the concrete cover, and support the wedging action caused by the bar's ribs, which indicates enhanced bond resistance [11–13]. Low workability is the main feature that may be accompanied by these superior cement composites, thus, additional precautions are considered. Using several types of admixtures with restricted content of coarse aggregate can be performed. For repair and strengthening purposes, these types of cement composites are more common due to their high cost, especially with massive quantities.

The bond strength of steel bars is also affected by the concrete cover as well as the spacing between the spliced bars. Not only the bond strength is dependent on the concrete cover and/or bar spacing but also the mode of failure can be switched [1,2,14,15]. Pullout failure is noticed for cases in which large concrete cover and bar spacing was provided, on the other hand, tensile splitting failure is observed for smaller concrete cover and bar spacing. It is worth mentioning that pullout failures can be detected with slightly noticed splitting cracks in case of providing proper confinement for the spliced bars [16]. Confining reinforcement (e.g. stirrups) restricts the growth of splitting cracks which contributes to increasing the bond strength of spliced/developed bars [1,2,17,18]. Increasing the amount of transverse reinforcement leads to higher bond strength and a splitting-induced failure can be altered to a pullout failure. However, additional confinement more than what is required does not improve the bond strength [2].

Headed bars, welding, mechanical splices, and hooks are several techniques that were used to enhance the performance of the conventional splice. Hooks/headed bars depend on the anchor at the end of the steel bar which suppresses its slippage. Welded splices reduce rebar congestion and improve concrete consolidation but it needs special equipment and qualified labor which means additional cost [19]. Using mechanical splices is one of the most effective methods for linking bars, but the high cost makes it a convenient method only for large bars' diameters. The bar's full strength can be transferred to concrete via headed bars with only a $4d_b$ length of splice [20]. Fawzy et al. [21] studied experimentally the conventional and the hook-ended splices, it was found that providing 180° hooks to the end of the spliced bars led to achieve the yield stress with splice length of $5d_b$, however, the conventional splice needed a splice length of $20d_b$ to achieve its yield stress. Abed et al. [22] studied nine RC beams having tension reinforcement with end anchoring headed bars. It was found that, the failure load of the headed bars compared to that of the non-headed bars achieved an increase of 98 % due to the additional bearing area provided by the headed bars. Conventional headed bars reduce the embedment length and simplify construction; however, concentrated stresses at the anchoring head can lead to a failure of the structural element [23].

As previously described, mechanical splices, welded splices, and headed bars have several drawbacks in the application, therefore, in this study a new technique namely plate-ended bars is developed as an anchoring system for reinforcing steel bars. To prevent the previously mentioned concentrated stresses induced by the headed bar, it is obvious that enlargement of bar's head will not be the optimum solution for concrete elements with dense reinforcement having spliced/developed bars. Therefore, in the current study, a unified plate was employed to anchor the end of the spliced bars. This plate can be designed with holes to host all spliced/non-spliced bars. This technique was established for the enhancement of the splice strength of steel bars embedded in HPC specimens. The current study focused on this splicing technique in HPC owing to its widespread in several long-span structures in which it is more predictable to have spliced reinforcement. The HPC in this study with low content of Polypropylene fiber was adopted to consider the workability, durability, and cost as it could be utilized for massive wide-span structures. In the current research, the experimental work was performed in two phases. For each phase, two sub-groups of specimens were carried out; a reference sub-group of straight-ended bars as well as a sub-group of anchor-ended bars. In addition, a parametric study was carried out using finite element modeling to study more parameters on the plate-ended technique. The outcomes of the parametric study were employed via statistical analysis to propose an empirical equation to estimate the splice capacity of plate-ended splices.

2. Experimental work

The experimental program of the current study was performed in two phases. The first phase (Phase I) is a set of splice specimens including straight-ended and anchor-ended bars embedded in concrete prisms and subjected to monotonic axial tension. Phase I was a preliminary study to assess the feasibility of the newly developed anchoring technique and was focusing on the strength gained by the splices with this developed system. The second phase (Phase II) is a series of RC beams including straight-ended and anchor-ended splices at the maximum tension zone under repeated loading. Phase II was a complementary study to investigate the flexural characteristics and ductility of splices adopting this anchoring system.

2.1. Test specimens

2.1.1. Axial tension specimens of Phase I

To avoid the drawbacks of the conventional pullout test reported by *ACI* 408R-03 [16], the configuration of test specimens in the current study in which both concrete and steel are subjected to tension was adopted. The bond strength obtained by this configuration showed variations within 10 % of the test results obtained by beam splice specimens having similar conditions [24–26].

In this research, an experimental study that included seven-lap spliced bars embedded in HPC concrete prisms without confinement was configured and tested. These specimens contained two pairs of lap spliced 12 mm diameter bars embedded in concrete prisms without transverse reinforcement. The specimens were subjected to axial tension. Specimens were classified into two sub-groups; straight-ended and anchor-ended. The first sub-group studied the conventional lap spliced bars with different lengths as a reference, as depicted in Fig. 1, while the other sub-group studied the anchor-ended steel bars at which the two pairs of bars were fixed into two opposite perforated plates. The configuration of the anchor-ended (plate-ended) bars is that a pair of bars were attached to a perforated steel plate, while the other pair of

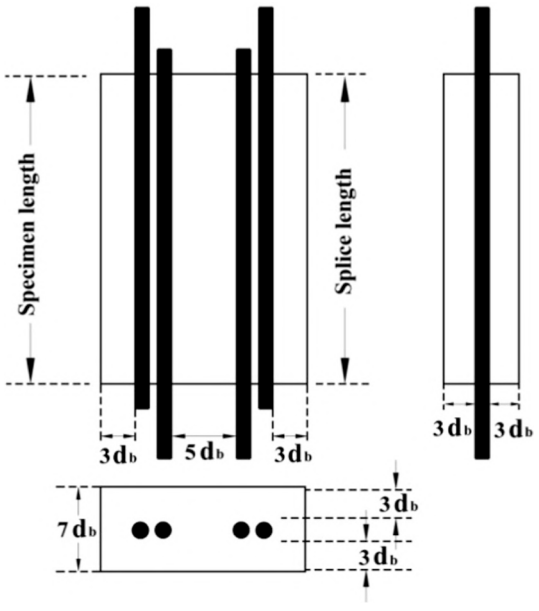


Fig. 1. Configuration of conventional lap splice for specimens S-O.

bars were inserted throw the holes of the same plate to be attached to the opposite perforated plate as shown in Fig. 2-a. The bars were attached to the perforated steel plate by welding to the plate's rear face to avoid the effects of heating on the tensile characteristics of the bars within the splice zone as depicted in Fig. 2-b. The perforated steel plates and the bars' distribution of a plate-ended specimen is shown in Fig. 3. The dimensions of the anchoring plates were selected to facilitate the application in the laboratory. At least 10 mm clear space was left between the borders of both the steel plate and the concrete specimen to allow the concrete to flow around the plate. The plate's thickness was selected equal to the bar's diameter to guarantee sufficient rigidity of the chosen plate. Therefore, the plate's dimensions adopted in Phase I were 60 mm × 160 mm × 12 mm.

Table 1 summarizes the dimensions of the concrete prisms as well as the lengths of splices for each sub-group. The nominal 12 mm diameter of the reinforcing bar was the basis to obtain all dimensions in Table 1. The concrete cover was selected intentionally as $3d_b$ for all test specimens of Phase I and Phase II, which is commonly followed in the practice of RC beams in the Middle East region. The system adopted for the notation of specimens shows the testing parameters; where for specimen X-Y-Zd; "X" indicates the type of specimen ("S" is for specimens of Phase I and "B" is for beams of Phase II), "Y" refers to the sub-group (O = straight-ended bars and P = plate-ended bars) and "Z" is the splice length in term of bar diameter (5, 10, 20 and 30 d_b). The test specimens of Phase I having the conventional splice (straight-ended) were designed as per *ACI* 408R-03 [16] to exhibit a bond failure. It was predictable that the anchor-ended specimens require less splice length compared to the straight-ended to transfer the design force of the bars, thus, a splice length of $5d_b$ was added to the sub-group of anchor-ended specimens to investigate its behavior. Out of the splice zone, the plates were covered by concrete with a thickness of three times the bar's diameter ($3d_b$), along this length the bars were isolated by bond-breakers to keep the bonded zone between the plates for all specimens.

2.1.2. Beam specimens of Phase II

The main purpose of this phase is to study the flexural behavior of RC beams containing the same lap splices of Phase I. Seven large-scale RC beam specimens with mid-span tension lap splice as well as two control beams without splice were configured and cast. The test beams had the same geometrical dimensions and reinforcement detailing which were provided to assure flexural failure. For all test beams, the main steel was

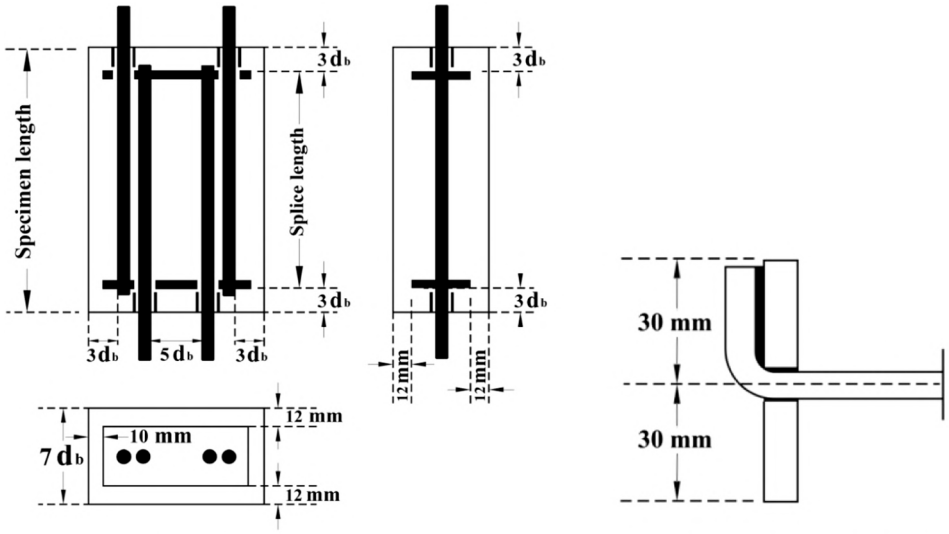


Fig. 3. Steel distribution of a plate-ended specimen.

Table 1
Dimensions of test specimens and beams.

Group	Sub-group	Splice length as a multiplier of bar diameter	Specimen notation	Prism/Beam dimensions (mm)		
				Length	Width	Depth
S	O	10 d_b	S-O-10d	120	180	84
		20 d_b	S-O-20d	240		
		30 d_b	S-O-30d	360		
	P	05 d_b	S-P-05d	130		
		10 d_b	S-P-10d	190		
		20 d_b	S-P-20d	310		
		30 db	S-P-30d	430		
B	Control	–	W-F	Total length of beam = 2400, Center-to-center span = 2100 mm	150	Total depth of beam = 300 mm
		–	W-D			
	O	05 d_b	B-O-05d			
		10 d_b	B-O-10d			
		20 d_b	B-O-20d			
		30 d_b	B-O-30d			
	P	05 d_b	B-P-05d			
		10 d_b	B-P-10d			
		20 d_b	B-P-20d			

O = straight-ended spliced bars; P = plate-ended bars.



(a) Dimensions of the plate-ended specimens.

(b) Anchor steel plate, the bar is welded to the plate's rear face.

Fig. 2. Configuration of the plate-ended specimens S-P.

two deformed steel bars of 12 mm diameter, while the secondary steel was two deformed steel bars of 10 mm diameter. To avoid shear failure, proper vertical stirrups were placed in the shear span zones of the beam. Following Phase I, the beams were classified into two main sub-groups, the first sub-group contains four beams at which the conventional lap splices with different lengths were studied as a benchmark, while the other sub-group consists of three beams with plate-ended spliced bars with different splice lengths. The specimens of Phase II were designed based on the experimental results of Phase I. For anchor-ended beams, the splice length of $30d_b$ was omitted in Phase II as it was not expected (regarding Phase I) to show a different behavior compared to the shorter splices of the same sub-group. On the other hand, a splice length of $5d_b$ was added to the straight-ended beams to be compared with its counterpart of the anchor-ended beams. The dimensions of the anchoring steel plates of Phase II followed the same previously mentioned configuration of Phase I, thus, the plate's dimensions adopted in Phase II were 60 mm × 130 mm × 12 mm. For control beams, one of them was tested under force-controlled mode and the other was tested under the displacement-controlled scheme, these two beams were notated as W–F, and W–D. The other beams follow the same previously illustrated notation system of Phase I. Table 1 summarizes the dimensions and splice lengths of all beams. For all test beams, the minimum side and lower concrete cover of the main steel were three times the main steel bar's diameter (the same cover of Phase I). The beams' geometry and reinforcement details are depicted in Fig. 4.

2.2. Steel bars/plates properties

The used reinforcement was deformed steel bars with a nominal yield stress of 400 MPa as commonly used in practice in the Middle East region. To obtain the mechanical properties of steel bars, three typical samples of steel bars were collected and then tested per ASTM A370 [27]. The effective area of the bar's cross-section (A_b) was estimated by dividing the bar's weight by the density of steel then concluding its volume and diameter. The average mechanical properties and geometric features of the tested samples are summarized in Table 2. For steel plates, the nominal yield and ultimate strengths were 360 and 520 MPa, respectively.

Table 2
Steel bars geometry and mechanical properties.

Property	Splice bar
Nominal diameter, d_b (mm)	12
Core diameter, D (mm)	12
Average rib depth, h_r (mm)	0.9
Rib spacing, s_r (mm)	8.5
Rib face angle, θ (^{O})	37
Relative rib area, R_r	0.1125
A_b (mm^2)	114.7
Average Young's modulus, Es (GPa)	207
Average yield strength, f_y (MPa)	463
Average ultimate tensile strength, f_u (MPa)	641
Maximum strain (%)	12.7 %

2.3. Mechanical properties of concrete

In the current research, to consider the enhancement in performance for both the workability and the dry shrinkage resistance, the adopted concrete mix contained a low volumetric ratio (0.2 %) of Polypropylene fibers. The same concrete mix was utilized in both the two phases of the experimental work for all tested specimens and beams. The concrete mix design adopted in this research was the same mix used in previous research [28]. The ingredients of the concrete mix are as follows; (1) ordinary Portland cement of grade 52.5, (2) fine aggregates, (3) dolomite coarse aggregates, (4) silica fume with average diameters ranging between 0.1 μm to 0.3 μm, (5) polypropylene fibers, (6) superplasticizers and (7) clean water. The length of the used polypropylene fibers (Fibermesh 300) according to the manufacturer's datasheet, is about 12–19 mm length with a tensile strength of about 386 MPa and elongation of about 13.2 %. These ingredients per cubic meter (kg/m^3) are summarized in Table 3. Precautions were taken into consideration to ensure bar alignment inside the wooden forms during casting in both two phases of the experimental work. With moderate vibration and satisfactory consolidation, the concrete was poured. After casting the

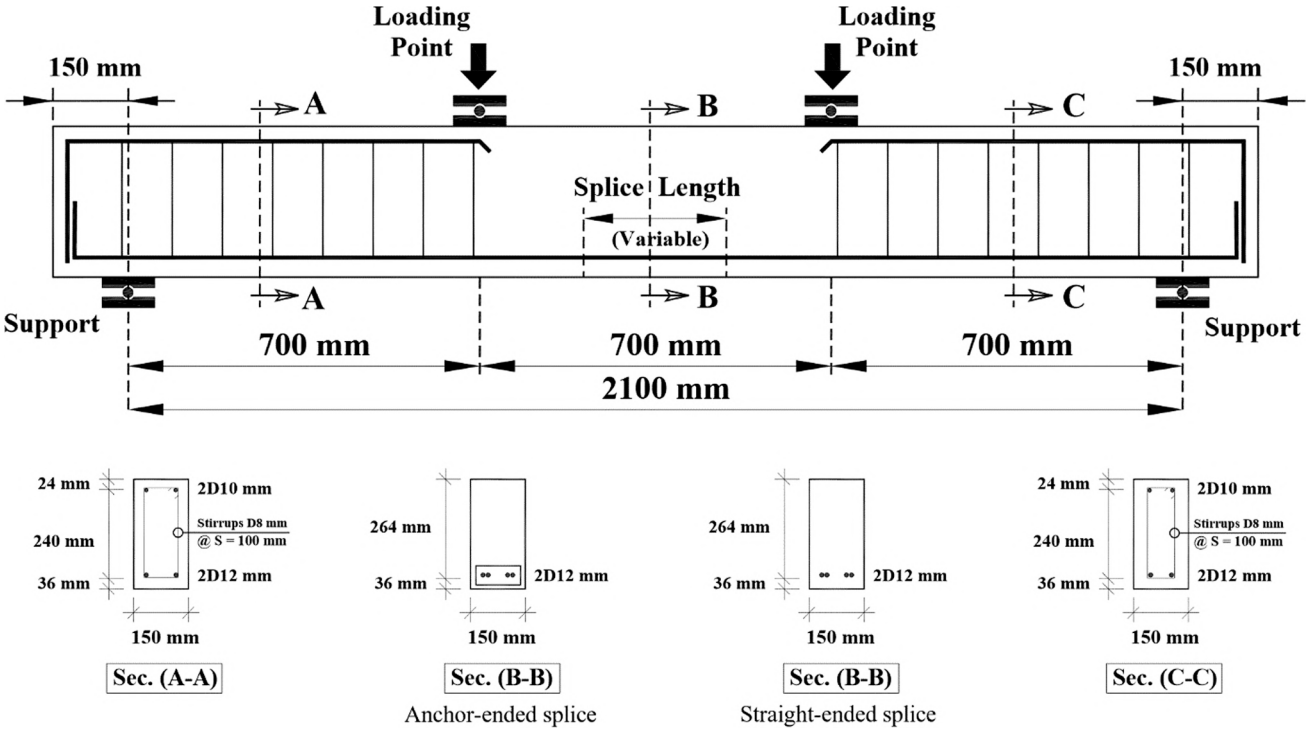


Fig. 4. Dimensions and reinforcement details for beams of Phase II.

Table 3
Ingredients of the concrete mix (kg/m^3).

Cement	Water	Water-to-cement ratio	Sand	Dolomite	Silica fume	Super plasticizer	Polypropylene fibers
450	135	0.3	535	1279	45	4.5	1.8

specimens, it was covered by wet textile, then the curing process began and continued for seven days.

Concrete cylinder compressive strength f_c' was determined from testing of 150 × 300 mm standard cylinders according to ASTM C39 [29]. Brazilian test was performed to obtain the indirect tensile strength f_t of concrete. Three standard cylindrical samples were prepared for each sub-group and then later tested on the same day as testing specimens of this sub-group. Table 4 reports the concrete compressive and tensile strengths of each sub-group. The tensile strength of the used concrete with low fiber content lies within the normal ranges compared to its compressive strength.

2.4. Test setup and instrumentation

2.4.1. Phase I

The specimens of Phase I were prepared to be tested until failure under axial tension force. Splice bars were connected to a rigid system of steel caps via steel grips and wedges to ensure the same displacement for both of the spliced bars. The rigid caps were tested against bare bars, and the caps deformation at its midpoint was found to be less than 0.3 mm. To have the best attachment between bars and grips, preloading up to 5 kN and then releasing was performed before the test. The capping system was connected to the thick plate of the hydraulic actuator with rigid screws.

To guarantee equal stress in both of the bars during the test, one strain gauge outside the specimen was mounted for each bar. Four LVDTs (Linear Variable Differential Transformer) having 50 mm gauge length were attached to the surface of the specimen perpendicularly to the axis of the splice to measure splitting cracks if any, as depicted in Fig. 5. In the case of specimens containing straight-ended splices, two LVDTs (one per each bar) were mounted at the back of the concrete prism to measure the relative movement (slip) of the free end of the spliced bar. The outputs (load and displacements) were measured and recorded via a data acquisition system connected with the actuator. The failure was expected to be sudden and violent, thus, a slow-motion high-definition video camera of 120 frames per second was used to record the tests. Fig. 5 shows the test set-up and the instrumentation.

2.4.2. Phase II

All beams of the second experimental phase were prepared to be tested in the form of a four-point loading scheme. A hydraulic actuator with a built-in load cell and a rigid spreader steel beam was used to apply-two concentrated loads on the tested beams. LVDTs and electrical resistance strain gauges were used to measure displacements and strains. For all tested beams, three LVDTs were used at mid-span and under concentrated loads as well as two strain gauges were mounted beside the splice at the zone of the maximum moment. Since the failure of splice specimens is violent, safety precautions were considered in the lab during the testing of beams of Phase II. Steel rods and pedestals were

Table 4
Compressive and tensile strengths of concrete for each sub-group.

Subgroup	f_c' (MPa)	f_t (MPa)
S-O	54	4.7
S-P	58	5.1
W*	56	4.8
B-O	56	4.8
B-P	57	5.1

* indicates that the beams without splices (Control beams).

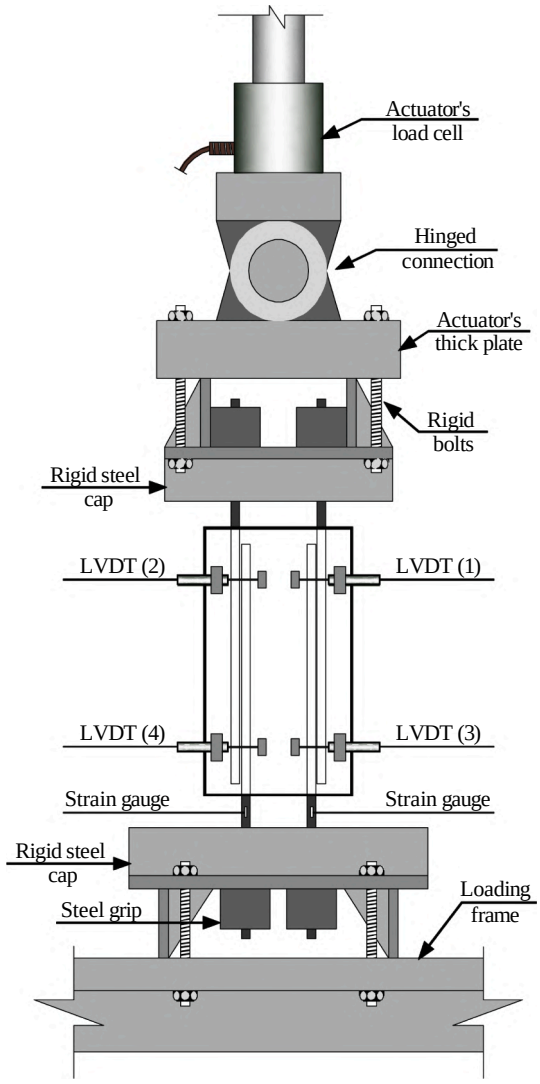


Fig. 5. Test setup and instrumentation, specimens of Phase I.

placed in front and under the beams to prevent accidents that could be caused by sudden and violent failure. White paint was sprayed on the beams' faces to assure a clearer view during observation of the cracks. The records of loads and displacements were collected using a data acquisition system connected with the actuator. Fig. 6 describes the test setup and instrumentation.

2.5. Loading protocol

For specimens of Phase I, axial tension tests were performed with a constant rate of monotonic loading. The axial force was applied on the upper pair of bars with a steady rate of about 5 kN/min up to failure. The beams of Phase II were tested under growing repeated loading until failure. The loading procedure involved nine rising stages; every stage consists of 5 loading cycles. The control beam's ultimate capacity was analytically estimated, and the total applied load was found to be about 90 kN. Subsequently, the upper and lower limits of each stage of loading

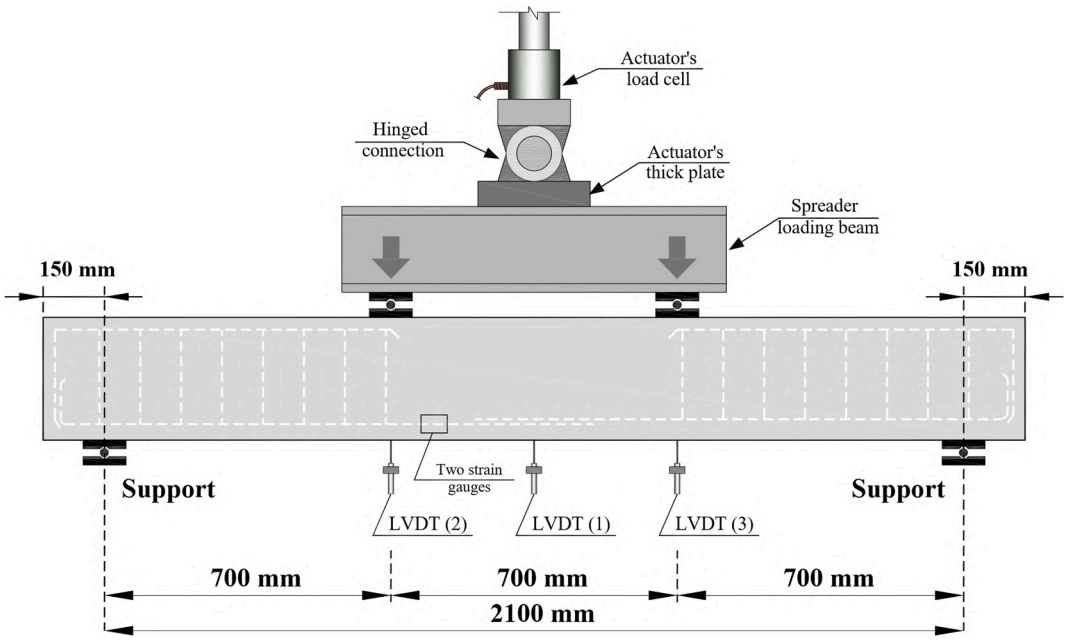
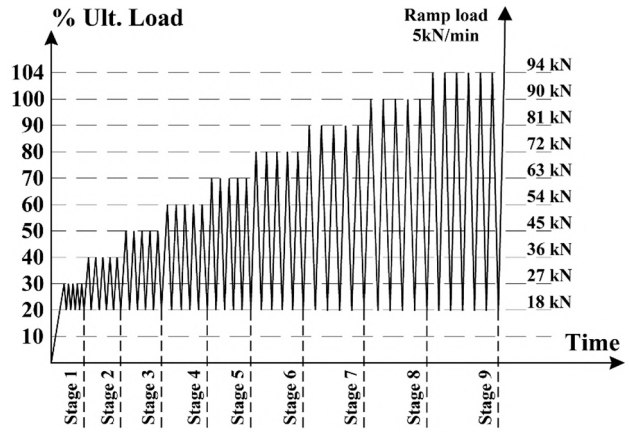


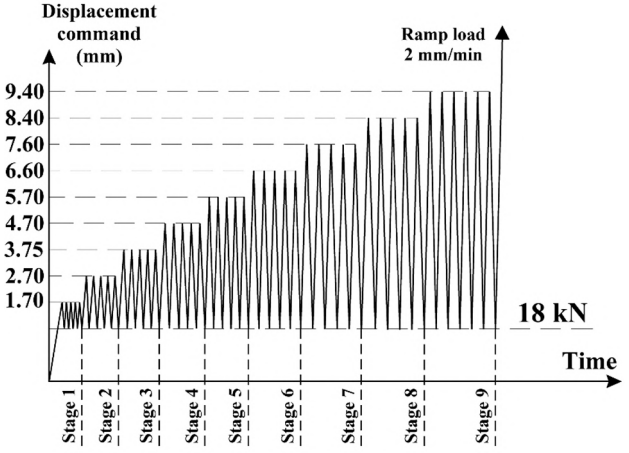
Fig. 6. Test setup and instrumentation, beams of Phase II.

were obtained as a percentage of this approximate estimated ultimate load. The upper loading limit was growing at every stage; however, the lower loading limit was constant (about 20 % of the estimated ultimate load). The first stage's upper limit started with 30 % of the estimated ultimate load; this upper limit was increasing by 10 % for each following stage until reaching finally 104 % of the predicted ultimate load.

For safety considerations of the sudden bond failure, the upper limit of the load was applied on the beams of Phase II using a displacement-controlled mode. To estimate the displacements of the upper limits, beam W–F was tested via force-controlled mode to obtain the accompanied displacements in each loading stage. The estimated displacement-controlled procedure involved two loading steps, a displacement-controlled loading step, and a force-controlled releasing step. The releasing step was force-controlled to avoid actuator-to-beam separation induced by the effect of the permanent plastic deformation of the beam. If the tested beam succeeded to overcome the ninth stage, the loading protocol was turned into a monotonic load with a constant rate of loading of about 2 mm/min until failure. Fig. 7-a shows the force-controlled time-dependent loading procedure, while, the time-dependent displacement-controlled procedure is described in Fig. 7-b.



a) Force-controlled loading protocol.



b) Displacement-controlled loading protocol.

Fig. 7. Loading protocols for beams of Phase II.

2.6. Results and discussion – Phase I

In the first phase of the experimental study, the experimental outcomes were discussed in terms of the ultimate load, maximum developed bond stress, modes of failure, and eventually the bond-slip response of the straight-ended specimens.

2.6.1. Ultimate load and the developed bond stress

The maximum load at failure for the splice bar (F) was recorded then the bar's tensile stress (f_s) is obtained by dividing the maximum load (F) by the average area of the bar's cross-section (A_b). The optimum development length of a splice is the length at which the tensile stress of the bar achieves yielding stress. Therefore, the maximum bar's tensile stress at failure (f_s) was compared to the bar's yield stress in terms of (f_s / f_y) to judge the efficiency of splice E_f. The bond stress is assumed to be uniformly distributed along the splice length then bond stress per unit length at failure (U_s) is estimated. To calculate the maximum developed bond stress, the bar force at failure was divided by the surface area of the bar within the splice length as follows [16,26]:

$$U_s = F/\pi * d_b * L_s \quad (1)$$

where F = the failure load of the splice bar, L_s = splice length, d_b = bar's diameter.

Table 5 summarizes the test results in addition to modes of failure. Specimens of straight-ended splices with lengths of 10, 20, and $30d_b$ achieved tensile stress of about 265, 517, and 576 MPa, respectively. On the other hand, all plate-ended specimens of 5, 10, 20, and $30d_b$ achieved the maximum potential strength of steel bars and exhibited rupture of reinforcing bars at tensile stresses of about 634, 633, 604, and 621 MPa, respectively. The rupture of steel bars of all plate-ended specimens was attributed to the anchoring effect of the attached plate which restricted the slippage of the bars until reaching their maximum tensile strength. Although S-P-20d recorded the lowest tensile stress among the plate-ended specimens, the failure was at the ultimate tensile strength of the bar and just varied by about 5 % from the maximum stress attained by S-P-05d. These variations in ultimate tensile strength can be considered acceptable within the different samples of steel bars. As listed in Table 5, the efficiency of the splice was judged, the lowest value was of the straight-ended splice of $10d_b$ as it failed before reaching the design stress (f_y) of the bar, while the other straight-ended splices of 20 and $30d_b$ failed beyond the yield point. The highest efficiencies were recorded by the anchor-ended specimens at which not only the yield point was exceeded but also the rupture of reinforcement was attained. The corresponding ultimate bond stress was 6.71, 6.55, and 4.86 MPa for straight-ended specimens with splice lengths of 10, 20, and $30d_b$, respectively. Specimen S-O-30d showed a lower value of the maximum developed bond stress compared to the other specimens of S-O. This is caused by the effect of the non-uniform distribution of bond stress along the splice length [30]. Generally, in the case of the same splice lengths, it is obvious that the anchoring technique of plate-ended specimens enhanced their capacities more than those of the straight-ended.

2.6.2. Modes of failure

Bar pullout accompanied by a shear crack and/or local concrete crushing were observed for all specimens of S-O as shown in Fig. 8. Specimen S-O-10d failed before achieving the yield of steel bars, while other specimens of S-O failed after reaching yield stress. Splitting cracks were not noticed during testing owing to the effect of the large thickness of the concrete cover ($3d_b$). The anchoring technique used for S-P not only changed the ultimate load but also modes of failure were affected. For all anchor-ended specimens, the newly developed technique of plate-ended bars was effective and led to a failure away of the splice, rupture of reinforcing bars at the maximum potential strength of steel bars was exhibited. During the test of plate-ended specimens, the slip-induced moving plates converted the tension force of bars into compression force acting between the plates. This action played a major role in suppressing the direct tension cracks of concrete during testing, especially in short lap splice specimens (S-P-5d and S-P-10d). These short splice specimens remained without cracking till the complete failure as shown in Fig. 9-a. The force transfer and compression force created between the bearing plates are depicted in Fig. 9-b.

Table 5
Test results of lap splice specimens.

Group	Sub-group	Specimen notation	Max. load (kN)	f_s (MPa)	U_s (MPa)	E_f (f_s /f_y)	Mode of failure
S	O	S-O-10d	60.9	265	6.71	0.58	P
		S-O-20d	118.7	517	6.55	1.12	YP
		S-O-30d	132.1	576	4.86	1.25	YP
	P	S-P-05d	145.5	634	–	1.33	R
		S-P-10d	145.2	633	–	1.33	R
		S-P-20d	138.6	604	–	1.27	R
		S-P-30d	142.4	621	–	1.3	R

f_s = the tensile stress developed in the reinforcing bars, U_s = the bond stress per unit length at failure, f_y = actual yield stress of steel, E_f = the efficiency of splice, P = Pullout of reinforcing bars, YP = Yielding of steel followed by pullout of bars, R = Rupture of reinforcing bars.



Fig. 8. Bars pullout followed by concrete crushing, specimen S-O-20d.

2.6.3. Bond-slip response

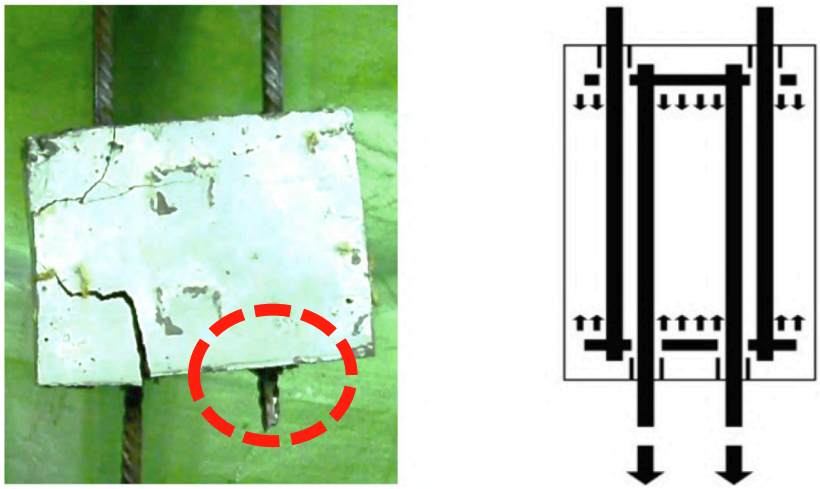
For straight-ended specimens, the bar-concrete relative displacement at the bar's free end (slip) was measured during the test. Therefore, the relationship between the bond stress vs slippage at the bar's free end was plotted. Fig. 10 shows the bond vs slip relationship for straight-ended specimens with splice lengths of 10, 20, and 30 d_b. In general, it can be noted that the bond stress of sub-group S-O at which all specimens failed by the pullout of bars showed an obvious sudden drop after the peak stress. This is attributed to the absence of confining reinforcement which contributes to equilibrating the bursting forces induced by the bond action. On the other hand, a minor portion of bond strength induced by tension stiffening of concrete is maintained because the tensile strength of concrete does not be lost instantly after cracking [31,32]. The minor residual bond strength vanishes suddenly after the widening of the cracks. It was clear that specimens with splice lengths of 10 and $20d_b$ showed approximately similar behavior, while, the longer splice of $30d_b$ length showed a different response. That can be attributed to the effect of the non-uniform distribution of the bond stress along the splice which becomes clearer as long as the splice length is longer.

2.7. Results and discussion – Phase II

In the second phase of the experimental study, the experimental outcomes were assessed in terms of the ultimate load, maximum deflection, crack pattern, modes of failure, and the load–deflection response for all beams provided with either straight-ended or anchor-ended splices.

2.7.1. Crack pattern and modes of failure

The control beams exhibited flexural failure as expected with the far-reaching yield of the tensile steel bars. The first crack was initiated at the tension soffit near the mid-span section of the beam at a vertical load of about 25 kN. By increasing the loading level, the cracks continued spreading inside the middle third of the beam. The control beams started failing with tension steel yielding then ended with concrete crushing in the compression side near the beam's mid-span section. Beams W–F and W–D failed at vertical loads of about 94 and 92.8 kN, respectively, after



(a) Rupture of reinforcing bars at maximum tensile strength of steel for S-P-

(b) Compression force acting between plates for anchor-ended

Fig. 9. Failure characteristics and force transfer of anchor-ended specimens.

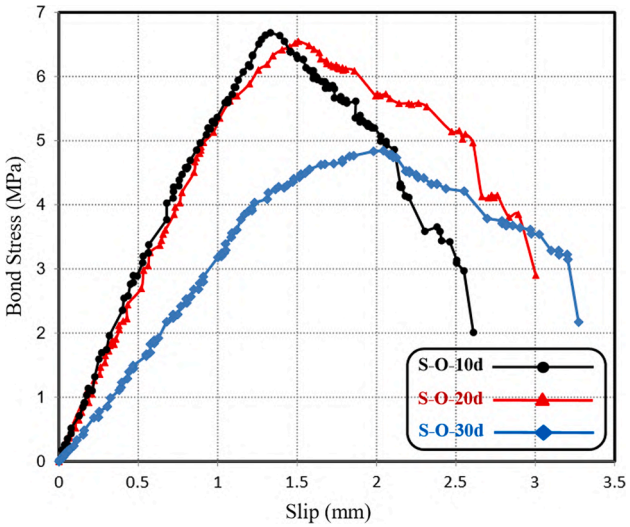


Fig. 10. Bond-slip relationship for specimens of S-O.

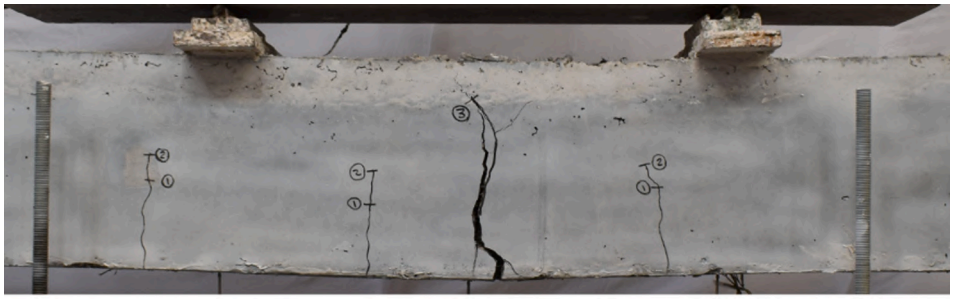
passing the ninth loading stage under the monotonic loading pattern with maximum displacements of about 63 and 64 mm, respectively. The control beams showed a ductile failure with the spreading of flexural cracks within the middle third. This ductile failure with high dissipated energy and without any noticed shear cracks near the supports is in complete agreement with the design of specimens. The cracking pattern of control beam W-D at failure is shown in Fig. 11.

For beams of sub-group B-O, during the loading process, the first flexural crack started to initiate at the tension side of the beam within the middle third. Generally, the first tension crack is initiated before the first loading stage for all beams of sub-group B-O at a vertical load of about 25 kN. Except for B-O-30d, all beams of sub-group B-O showed bond failure at different stages of loading. Beam B-O-05d failed after consuming two loading stages before reaching the third loading one. The observed cracks were only flexural cracks, no splitting cracks were observed due to the superior concrete cover $3d_d$. Just reaching a vertical load of about 39.8 kN with a mid-span deflection of about 4.1 mm, suddenly, the beam failed by bars pullout with an instant increase of the main flexural crack towards the upper edge of the beam due to the absence of tensile resistance. Fig. 12-a shows the cracking pattern of B-O-05d. For beam B-O-10d, failure took place after passing five loading stages before reaching the sixth loading one. After cracking load, the flexural cracks were observed and continued spreading inside the middle third of the beam until failure. The failure was triggered just at a vertical load of about 59.1 kN showing a mid-span deflection of about 7.2 mm. The beam failed instantly by the pullout of the main steel bars with a sudden widening of the major flexural crack due to the absence of tensile resistance of the main steel. Fig. 12-b depicts the cracking pattern of B-O-10d at failure.

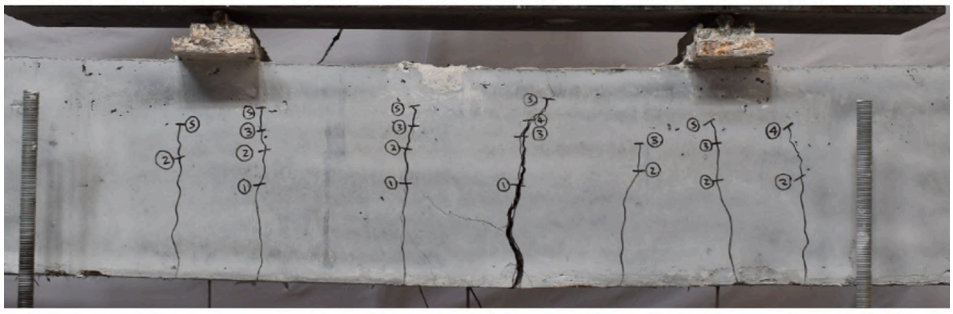
Beam B-O-20d failed after two cycles only in the ninth stage. The flexural cracks were noticed and spread at the maximum tension zone of the beam till the failure took place. The failure was started at a vertical load of about 83.7 kN showing maximum deflection at the mid-span of about 11.2 mm. The strain records indicated that the main steel yielded



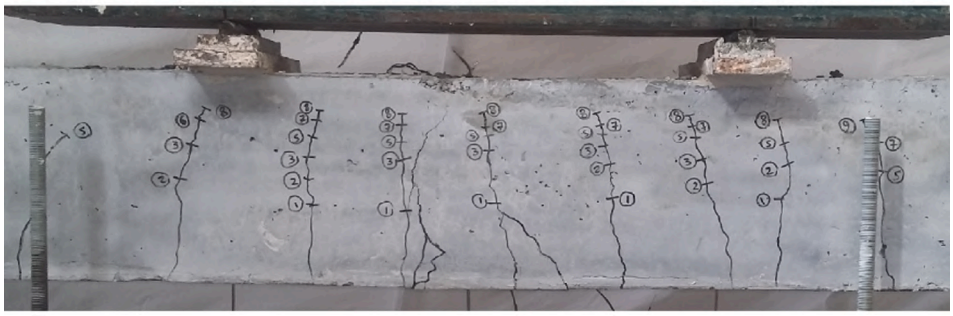
Fig. 11. Beam W–D at failure.



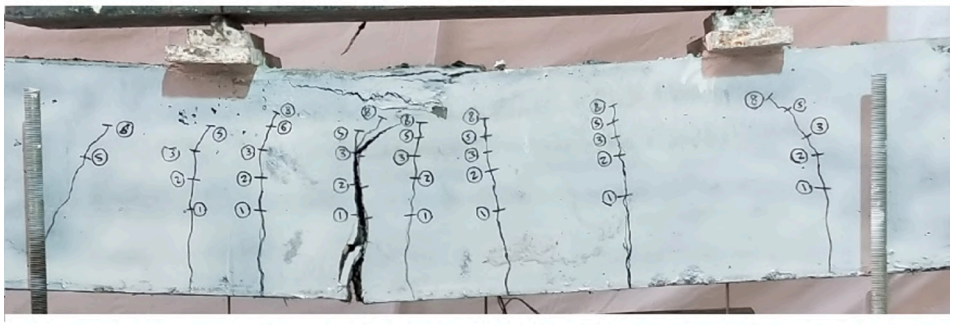
a) Crack Pattern of B-O-05d at failure.



b) Crack Pattern of B-O-10d at failure.



c) Crack Pattern of B-O-20d at failure.



d) Crack Pattern of B-O-30d at failure.

Fig. 12. Crack pattern of beams of sub-group B-O at failure.

before the loss of its bond with the surrounding concrete. Although the main steel reached its design force, the beam exhibited lower energy dissipation and lower maximum deflection compared to those of the control beam W–D. The failure was sudden due to the pullout of the main steel bars with an instant increase in the major crack width due to the loss of tension force carried by the main steel. The cracking pattern of B-O-20d is shown in Fig. 12-c. Beam B-O-30d failed during the monotonic loading stage. B-O-30d started failing after exceeding the yield stress of the main steel and subsequently ended with concrete crushing in the compression side at the beam's mid-span section. The beam failed in a ductile manner at a vertical load of about 91.1 kN showing maximum deflection at the mid-span section of about 61 mm. For straight-ended splice beams, the splice length of $30d_b$ was not only sufficient to transfer the design force of the main steel bars but also to

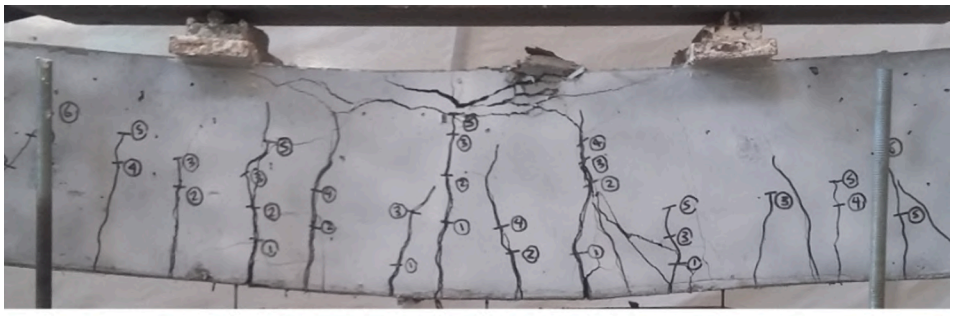
reach the same ductile manner of the beams without a splice. B-O-30d exhibited high energy dissipation and high maximum deflection similar to the control beam W–D. The cracking pattern of B-O-30d at failure is shown in Fig. 12-d.

For the anchor-ended beams, bearing plates were connected to the end of the lap spliced bars at the zone of the splice to prevent the expected slippage. Throughout the loading process, the first flexural crack started to initiate at the tension side of the beam at the middle third for all beams of sub-group B-P. Approximately, at a vertical load of about 25 kN, the first crack was noticed preceding the start of the first loading stage for all beams of sub-group B-P. This was the same cracking load of the sub-group of straight-ended bars which is accredited to the similarity of stiffness of all beams. Due to flexural stresses, all beams of sub-group B-P exhibited the same mode of failure. These bearing plates convert the tensile force of bars into a compression force between them which prevents any slippage or movement of the spliced bars. All beams of sub-group B-P failed after passing all loading stages during the monotonic loading. After the cracking load, the flexural cracks were obvious within the middle third of the beam up to failure. For beams B-P-05d, B-P-10d, and B-P-20d, ductile failures were recorded with ultimate loads of about 92.5, 93.2, and 92.1 kN, respectively, while the corresponding maximum deflections at mid-span sections were 64, 65, and 62.3 mm, respectively. These beams started the failure with a far-reaching yield stress of the main tensile steel followed by concrete crushing in the compression side near the beam's mid-span section.

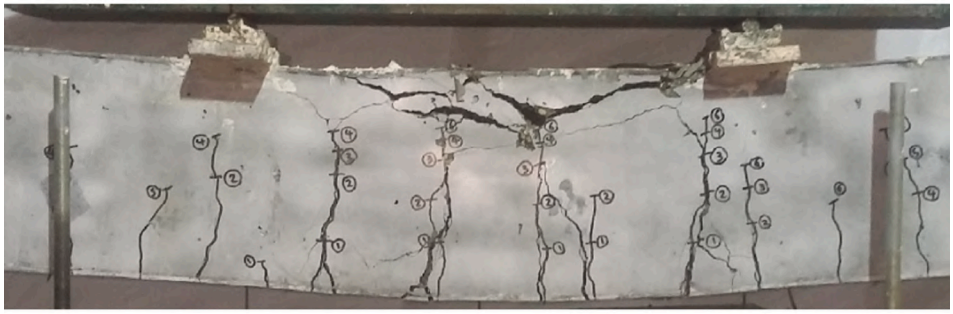
Similar to the control beam W–D, these beams recorded high energy dissipation as well as maximum deflection. The lap splice length of $5d_b$ for the end-plate technique was enough to transfer the design force of the main steel bars side by side with reaching the same ductility of W–D. It is necessary to mention that no tension cracks were noticed at the splice zone between the plates until failure; this may be caused by the plates' induced action of transforming the tensile forces of bars into compression between the plates. This action may form a compression field within the splice zone which prevented the initiation of tension cracks at this zone. The cracking pattern of B-P-05d, B-P-10d, and B-P-20d at failure are shown in Fig. 13. Table 6 summarizes the ultimate loads and maximum deflections compared to the control beam for splice lengths of 5, 10, 20, and $30d_b$.

2.7.2. Load-deflection response

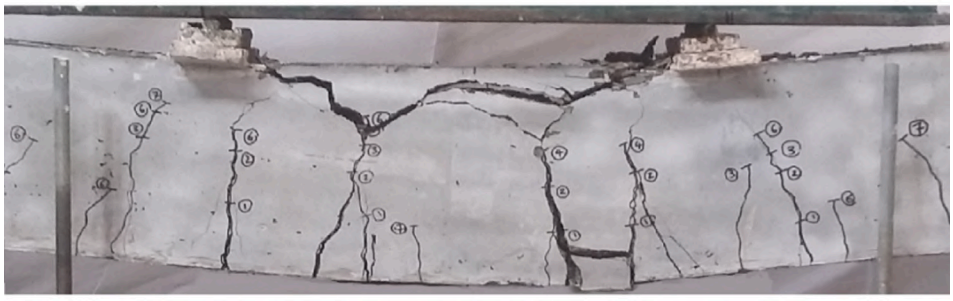
Generally, until the first flexural crack, all beams showed the same stiffness. Subsequently, a decrease in stiffness was triggered after the first flexural crack at a vertical load of about 25 kN before the first loading stage. At the beginning of the loading stages, it was obvious that



a) Crack pattern of B-P-05d at failure.



b) Crack pattern of B-P-10d at failure.



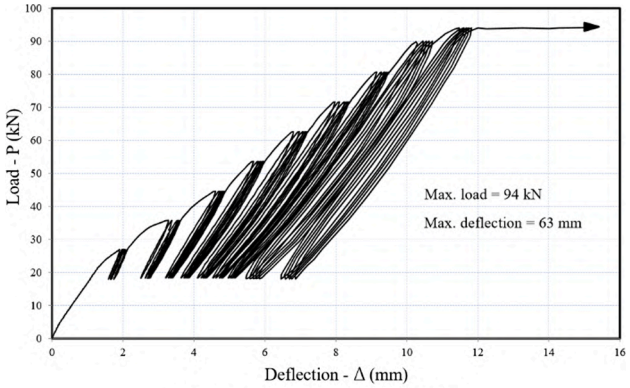
c) Crack pattern of B-P-20d at failure.

Fig. 13. Crack pattern of beams of sub-group B-P at failure.

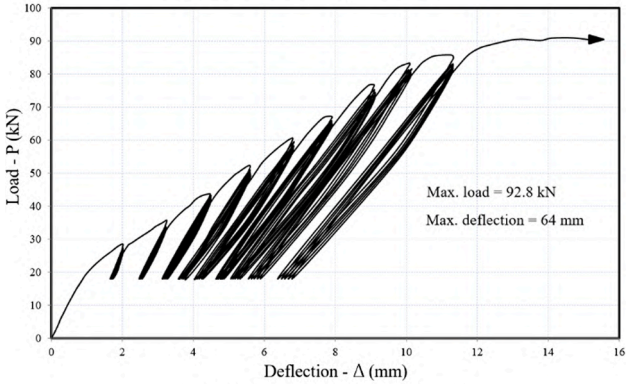
Table 6
Comparison between ultimate loads and maximum deflections for all beams and those corresponding to control beam.

% Max. deflection to control beam	% ult. Load to control beam	Max. deflection Δ (mm)	Ult. Load (kN)	Sub-group	Splice length
100	100	64.1	92.8	Control Beam	W–D
6.4	42.8	4.1	39.8	B-O	05 d_b
99.8	99.6	64	92.5	B-P	
11.2	63.7	7.2	59.1	B-O	10 d_b
101.4	100.4	65	93.2	B-P	
17.5	90.1	11.2	83.7	B-O	20 d_b
97.2	99.2	62.3	92.1	B-P	
95.2	98.2	61	91.1	B-O	30 d_b

all specimens were in the elastic range. At the early stages of loading, the areas enclosed by hysteresis loops were very small. With further loading, the beams went into the elastic–plastic manner with furthermore spreading of the cracks. Generally, it was noticed that, at the yield point of main tensile steel at a vertical load of about 70 kN, a slight decrease in flexural stiffness was recorded in load–deflection response. By accumulated damage, the beams were losing their stiffness gradually, subsequently, the area inside hysteresis loops increased in every following stage. Beams B-O-05d and B-O-10d failed instantly with a sharp decrease of stiffens after the second and the fifth loading stages, respectively, as shown in Fig. 15-a and 15-b. Beam B-O-20d just passed two cycles from the ninth interval before failure, just before the failure, deterioration took place in the beam's stiffness with obvious dissipation of energy in the last two cycles of loading as shown in Fig. 15-c. In the load–deflection relationship, for the other beams that succeeded to pass all stages of loading, a plateau interval was recorded before failure reached its maximum load and deflection. Significant energy dissipation

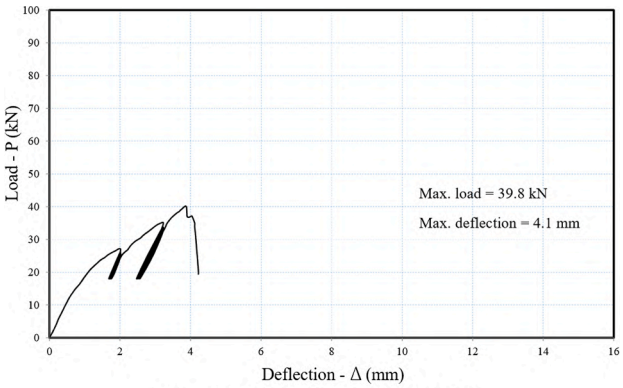


a) Load-deflection response of W-F.

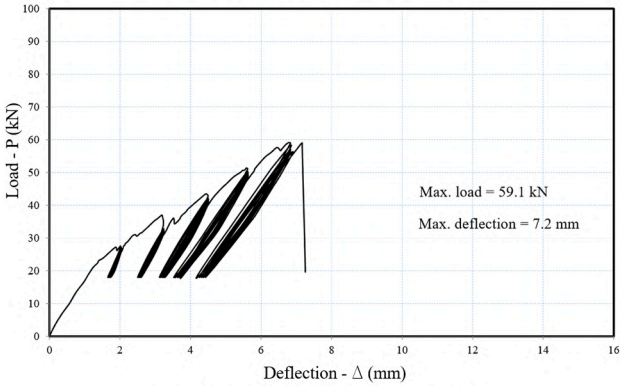


b) Load-deflection response of W-D.

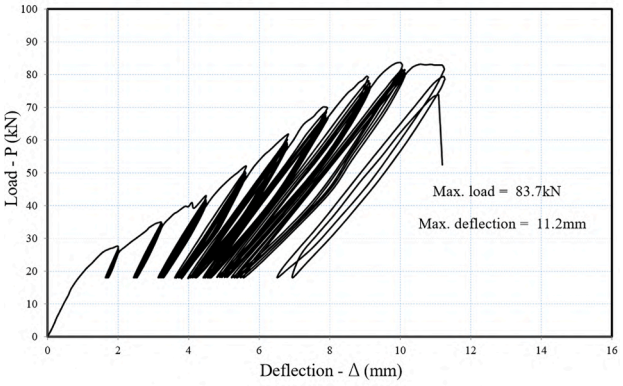
Fig. 14. Load vs mid-span deflection relationship of control beams.



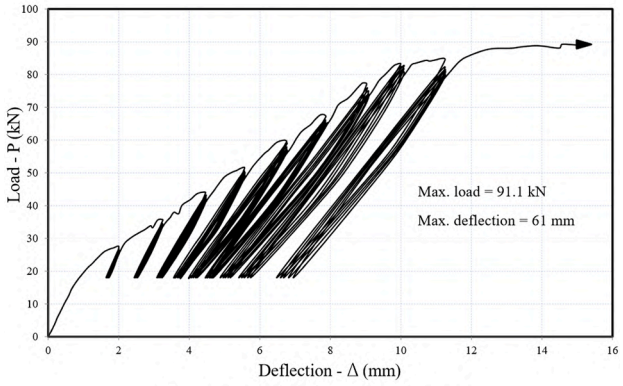
a) Load-deflection response of B-O-05d.



b) Load-deflection response of B-O-10d.



c) Load-deflection response of B-O-20d.



d) Load-deflection response of B-O-30d.

Fig. 15. Load vs mid-span deflection relationship of beams B-O.

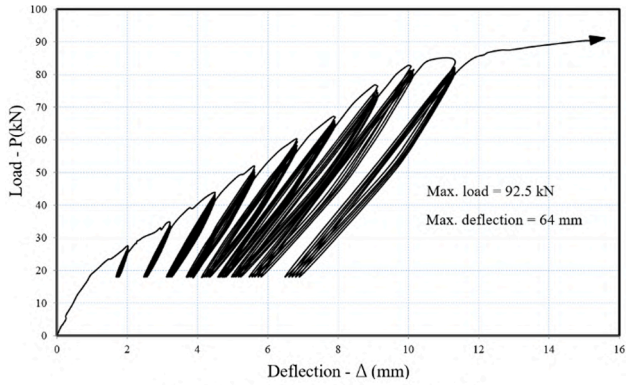
induced by this hysteresis manner was obvious during the loading–unloading processes. The load–deflection responses of all beams of Phase II are shown in Figs. 14–16.

3. Finite element modeling (FEM)

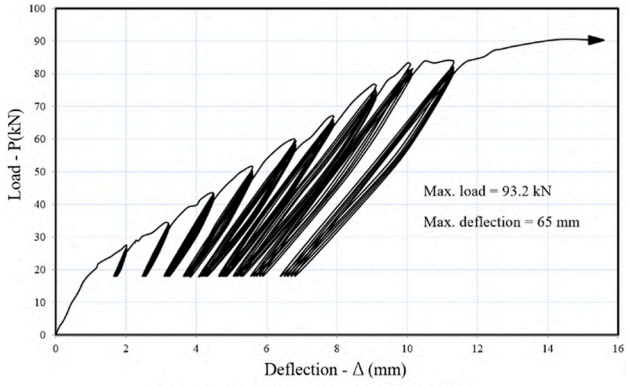
Since the failure of all anchor-ended specimens was out of splice, the failure induced by the anchor (plate) has to be further assessed. The rigidity of the used plates and the used concrete grade are the most effective parameters that should be studied in detail. In the current study, finite element modeling was employed for this purpose. ABAQUS software was used to model the specimens with the same configuration in Phase I tests.

3.1. Materials modeling

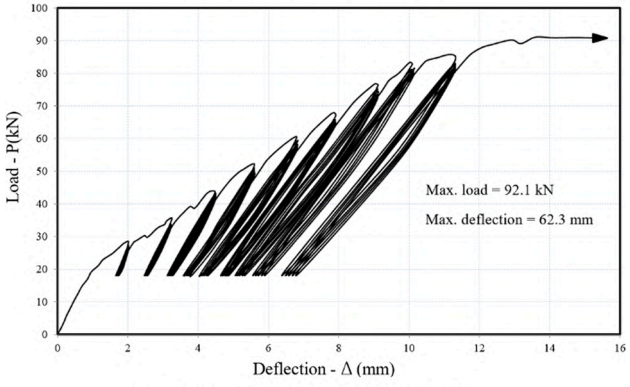
For concrete modeling, the "Concrete damage plasticity model" (CDP) is adopted. This model assumes that the failure modes are tensile cracking and compressive crushing [33]. For the concrete model, the relationship of uniaxial compressive stress–strain [34,35] is shown in Fig. 17, where f_c is the compression stress corresponding to the strain value ε_c and ε_o is the ultimate value of the strain of concrete. The Poisson's ratio of concrete was assumed to be 0.20. The tensile behavior of concrete under tension [36,37] is shown in Fig. 18, where f_t is the tensile stress, ε_t is the tensile strain, f_{cr} is the tensile strength and ε_{cr} is the accompanied tensile strain. The stress–strain behavior of steel was assumed to be a bilinear relationship in which the modulus of elasticity of steel E_s before yielding stress then it turns to 0.1 E_s after yield stress.



a) Load-deflection response for B-P-05d.



b) Load-deflection response for B-P-10d.



c) Load-deflection response for B-P-20d.

Fig. 16. Load vs mid-span deflection relationship of beams B-P.

3.2. Bond modeling

Bond is a critical factor in the relationship between the steel and the surrounding concrete as it provides the transferring shear between their surfaces for composite action. To model the interface shear of steel-to-concrete bond in ABAQUS software, the Cohesive Zone Model (CZM) was employed using the traction-separation law to allow bond failure mode. For proper simulation of the cohesive behavior, three features of the behavior have to be described. The first one is the linear elastic traction-separation stage, and the second is the point at which the damage initiates, and eventually is the damage evolution stage as depicted in Fig. 19. This model was adopted in previous research work [38,39]. The parameters of interface shear strength, fracture energy, and elastic shear stiffness have to be obtained from the experimental data of local bond-slip tests. In case the required experimental data is not available, there are many constitutive models to estimate the local bond-slip relationship.

Models for ribbed bars have been historically derived for "Good bond conditions" in which sufficient thickness of the concrete cover is provided to ensure a "pullout" failure mode. This clear pullout failure in which the bar pulls out of the concrete leaving a smooth hole but without an obvious splitting or damage to the cover. Other failures including splitting cracks or damage to concrete can be classified as "other bond conditions". In these other bond conditions, the failure takes place prematurely to the pullout failure. The CEB-FIP Model code [40] provided an idealized local bond-slip relationship as shown in Fig. 20. where; S_1 and S_2 represent the ultimate slip regarding the bond strength τ_{max} for pullout failure, S_3 the final slip at which the frictional bond stress is triggered, τ_f the residual frictional bond stress. In the current research, the parameters of interface shear strength (bond strength), fracture energy, and elastic shear stiffness were estimated regarding the idealized local bond-slip relationship provided by CEB-FIP Model code [40].

To represent the relationship between the steel plates and concrete, normal interaction was utilized. To define the normal interaction, the contact pressure-overclosure feature was selected as the "Hard-Contact" model in Abaqus/standard. In the Hard-Contact feature, penetration is

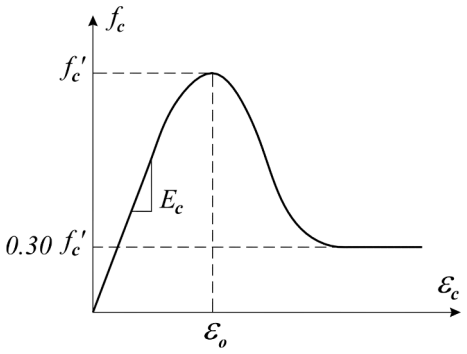


Fig. 17. Uniaxial compressive stress vs strain relationship of concrete, Saenz (1964).

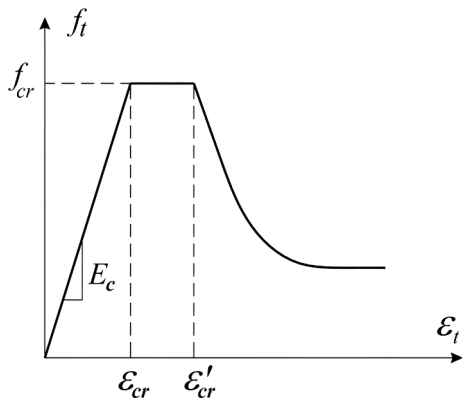


Fig. 18. Uniaxial tensile stress vs strain relationship of concrete.

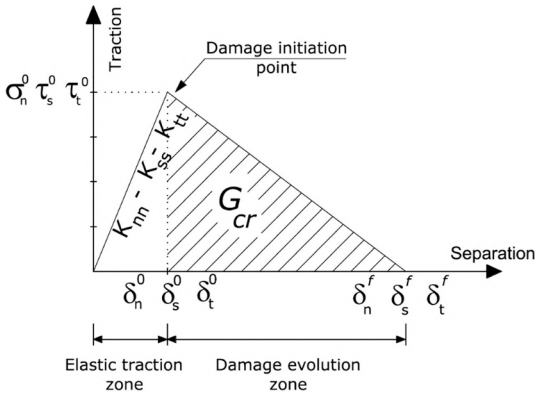


Fig. 19. The traction-separation relationship, Sakr et al. 2017.

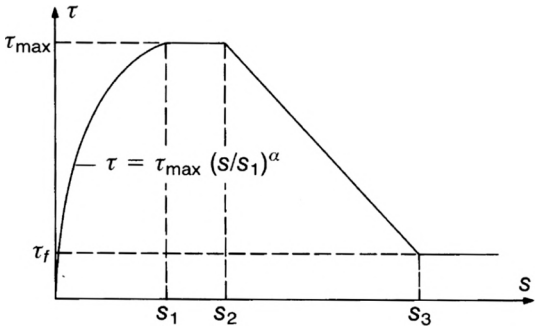


Fig. 20. Local bond-slip relationship for good bond condition (pullout failure), CEB-FIP Model code (1990).

not allowed for the master surface, in addition, there is no transmission of the tensile forces. Note that, the magnitude of contact pressures transmitted when the surfaces are in contact is unlimited. Since the plate was embedded in concrete and not allowed to move, tangential behavior was activated with a rough friction formulation at which no slip would occur once points are in contact to prevent sliding of the plate over the concrete surface.

3.3. Elements and meshing

8-node three-dimensional linear brick, reduced integration, hourglass control element, namely C3D8R, was used for both concrete, steel bars, and steel plates. To detect the proper meshing size, a sensitivity analysis has been carried out to evaluate the suitable and stable mesh size. For each specimen, a size-constrained automated meshing operation was applied with a limited size of the elements, the automated meshing provides the zones with stress concentrations (circular holes) with a fine meshing. For concrete elements, the solution tries were carried out with a maximum element size varies between 10 and 25 mm, while the steel bar was divided in cross-section into 8 sectors with a maximum longitudinal size that varies from 4 to 10 mm. For steel plates, the maximum element size lies between 4 and 10 mm. For each modeled specimen, several solution tries were carried out with different element sizes until reaching the best results compared to the experimental results.

3.4. Validation of the proposed model

To validate the proposed finite element model, a comparison has been done between the experimental results of the straight and anchor-ended specimens of Phase I and the outputs of their counterparts of modeled specimens. The geometrical details of the modeled specimens are previously described in Table 1 and Figs. 1, 2. The validated specimens included all straight-ended specimens and one specimen of plate-ended type (S-P-10d). The previously mentioned constitutive material models were used to represent the used materials in the current study. The uniaxial tensile and compressive stress–strain relationships of concrete were constructed based on the experimental work as the average concrete strengths were 54 and 58 MPa for straight and plate-ended specimens, respectively. The tensile stress–strain behavior of steel was also based on the experimental outcomes of steel tests as listed in Table 2. The steel plate's properties were based on the nominal yield and ultimate strengths of the used plates which were 360 and 520 MPa, respectively. The input data for bond characteristics were based on the local bond-slip relationship derived by CEB-FIP Model code [40] for unconfined concrete with "other bond conditions" where; $S_1 = S_2 = 0.60$ mm, $S_3 = 2.5$ mm, and $\tau_{max} = 7.4$ MPa. Based on this data, the shear stiffness per unit area (K_{tt}, K_{ss}) was obtained to be 12.3 N/mm. Damage initiation was defined in ABAQUS with a maximum shear strength of 7.4 MPa. For the damage evolution feature, the residual frictional bond stress τ_f was assumed to be zero at final slip S_3, subsequently, the fracture energy is the area under the softening branch of bond-slip and equals 7 N.mm. The finite element model was verified against the experimental work in terms of mode of failure, ultimate load, and the bond-slip response of straight-ended specimens.

3.4.1. Mode of failure

According to the experimental results, all specimens of straight-ended bars failed due to pull-out of reinforcing bars followed by local concrete crushing and/or shear failure as shown in Fig. 21 for S-O-10d.



Fig. 21. Slippage of bars accompanied with local concrete crushing and/or shear failure of S-O-10d.

The maximum principal plastic strain on the deformed shape obtained by numerical analysis of straight-ended specimen S-O-10d is shown in Fig. 22. The failure of the modeled specimens was characterized by a sudden loss of the tensile stress carried by the steel bars accompanied by an instant increasing large displacement at both free and loaded ends of the steel bars just after reaching the bond strength of the splice. The local concrete crushing following the pull-out failure was obvious in the distortion that took place in the concrete prism during failure as shown in Fig. 22. The mode of failure obtained by the experimental investigation is compared to that of the numerical analysis, the numerical and experimental results exhibited a similar mode of failure. Specimen S-P-10d failed at the test due to rupture of the reinforcing bar which coincides with the numerical simulation that showed the maximum bars' tensile strength of 640 MPa as shown in Fig. 26. The maximum tensile stress of bars is reached along the entire embedded length in S-P-10d which indicates that the role played by the plates to prevent slippage of bars is triggered by the failure of the bond strength along the splice length.

3.4.2. Ultimate loads

Comparisons between ultimate loads and bars' tensile stresses obtained from the experimental tests against that conducted from the numerical analysis are depicted in Figs. 23–26. The numerical modeling of specimens S-O-10d, S-O-20d, S-O-30d, and S-P-10d exhibited 87 %, 91 %, 90 %, and 99 % of the ultimate load compared to the experimental work with a maximum tensile stress of 232, 479, 523, and 640 MPa, respectively. These values show that the numerical ultimate load findings showed acceptable variations compared to that obtained by the experimental testing.

3.4.3. Bond-slip response

In the numerical analysis, the bond stress was estimated by dividing the maximum developed load by the bar's surface area along splice length following the method followed in experimental work. As shown in Fig. 27, the bond stress reached and the relevant relative displacements at the bar's free end (slip) in the numerical analysis were plotted and compared to these of the experimental tests. For specimens with 10 and 20d_b of splice lengths, the recorded peak bond stress was approximately the same despite the different maximum tensile load, this is attributed to the almost uniformly distributed bond stress along the development length. As shown in the figures, the response of load-slip obtained by numerical analysis showed a good tendency with the experimental plots.

3.5. Parametric study using FEM

Despite the failure of bond strength recorded along the splice length in the model of specimen S-P-10d, the bar's tensile stress reached its maximum value and failed by rupture. In addition, compressive stress

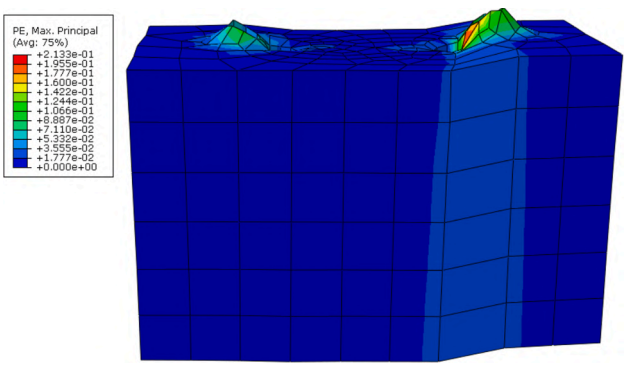


Fig. 22. Maximum principal plastic strain on the deformed shape of S-O-10d in ABAQUS model at failure.

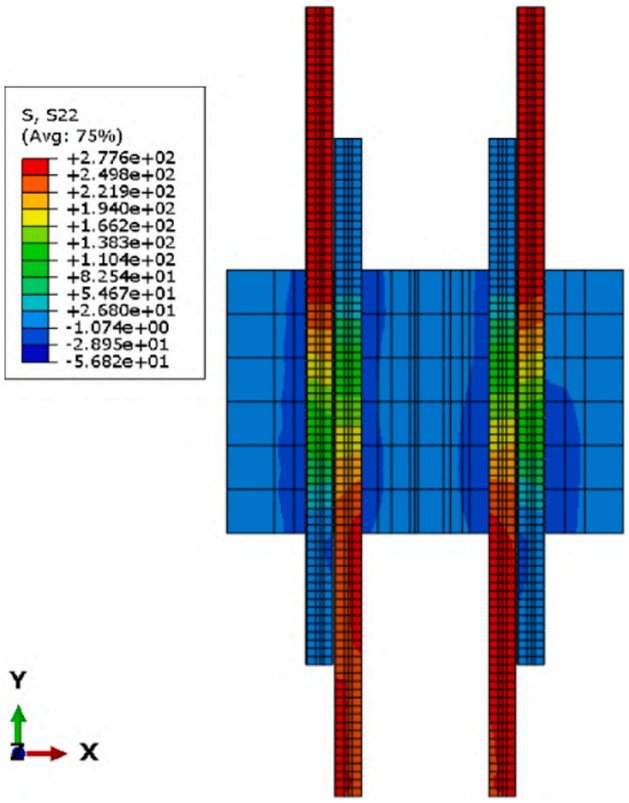


Fig. 23. Ultimate tensile stress obtained by numerical analysis of S-O-10d.

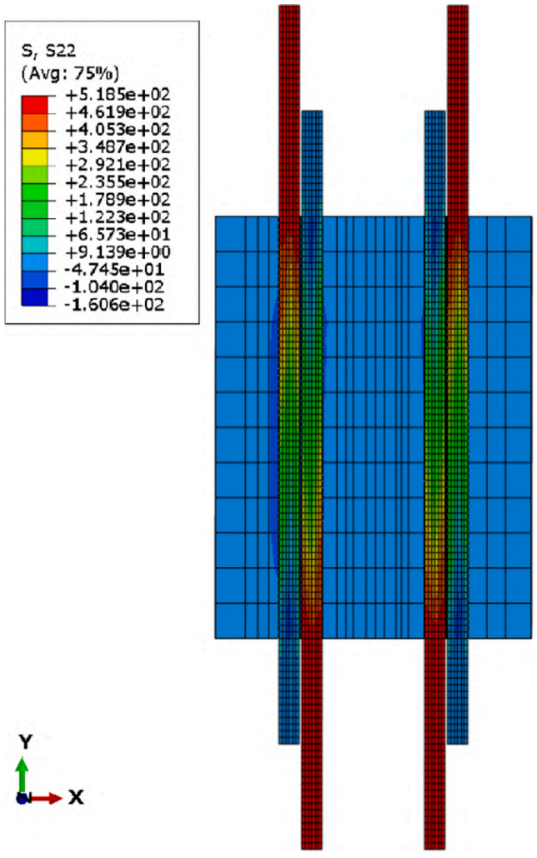


Fig. 24. Ultimate tensile stress obtained by numerical analysis of S-O-20d.

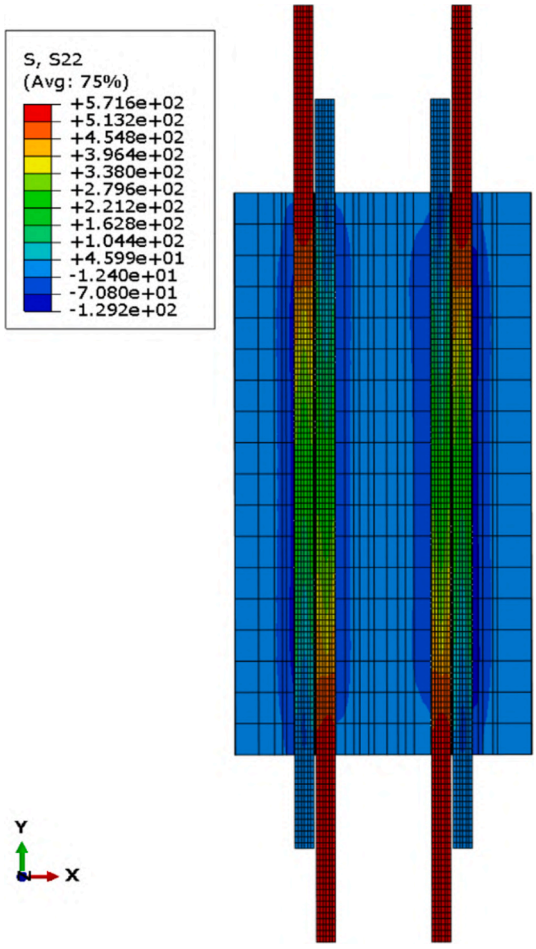


Fig. 25. Ultimate tensile stress obtained by numerical analysis of S-O-30d.

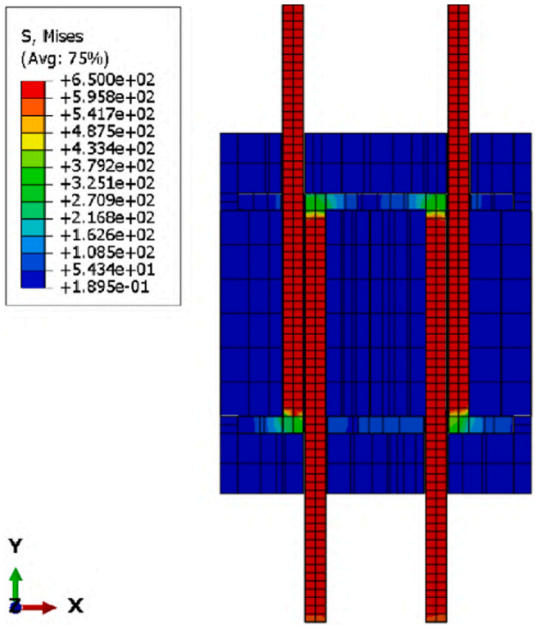
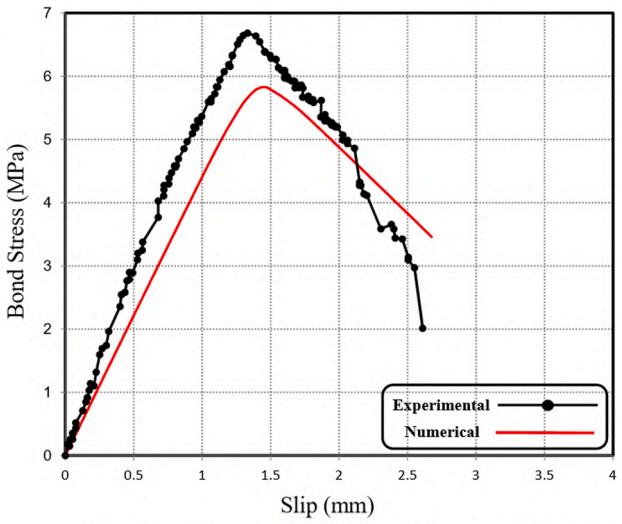
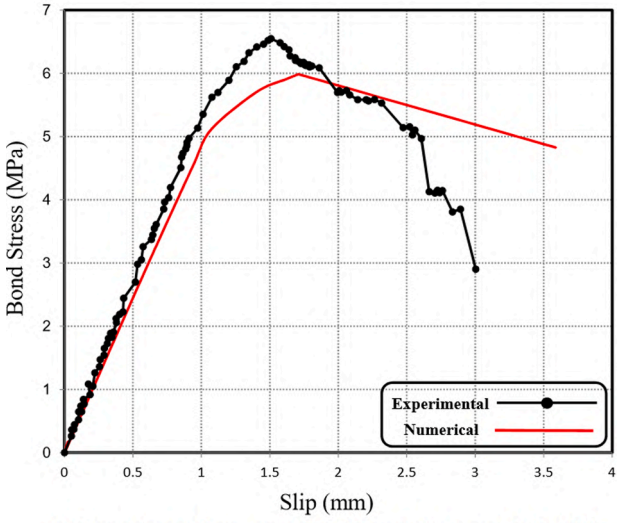


Fig. 26. Ultimate tensile stress obtained by numerical analysis of S-P-10d.

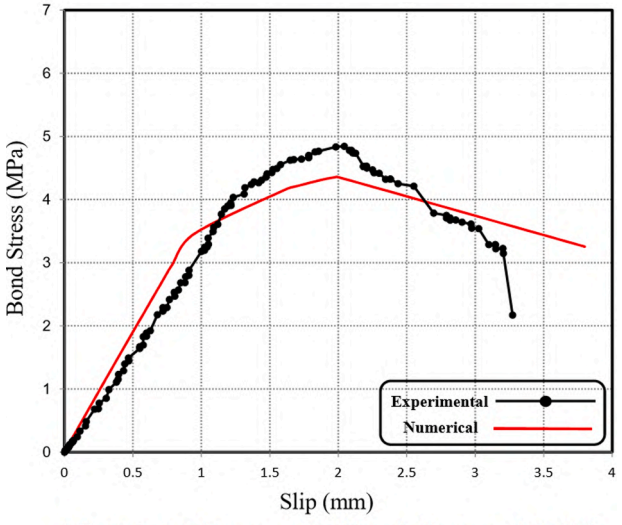
was observed in the concrete between the plates which means that the failure of these specimens has to be due to the crushing of concrete between the plates if it is not due to the maximum tensile strength of the



a) Experimental vs. numerical bond-slip crve, S-O-10d



b) Experimental vs. numerical bond-slip crve, S-O-20d



c) Experimental vs. numerical bond-slip crve, S-O-30d

Fig. 27. Experimental vs numerical bond-slip responses for specimens of S-O.

bars. The failure of plate-ended specimens is controlled by the resistance of the concrete between the plates. The stiffness of the plates also governs the distribution of this compressive stress between plates. The plate-ended specimens require further studying to recognize the parameters that may affect the behavior of these specimens. In this section, a parametric study is carried out to investigate several parameters that may affect the capacity of the plate-ended specimens, using the same configurations of specimens of Phase I under axial tension. The parameters are concrete strength, bar diameter, plate offset around the bars, and plate thickness.

In the parametric study, it was found that the anchored splices with high-strength concrete reach the maximum tensile strength of the bars even with tiny plate dimensions which is not applicable in practice. For studying purposes, to have a wide range of the plate's dimensions that enables to conduct of a design equation, normal to medium strengths of concrete were adopted in the parametric study; however, this technique is also suitable for any type of concrete.

Fig. 28 shows the suggested configuration of the plate. Where; S is the offset of the plate measured from the center of the bar and the plate's thickness is t_p. Three main groups of suggested specimens were classified according to the concrete strength (f_c'= 25, 40, and 55 MPa). Each main group with 36 suggested specimens is studying three bars' diameters (d_b = 12, 18, and 25 mm). For each diameter, three sub-groups are suggested at which the thickness of the plate is a variable (t_p/d_b = 0.40, 0.80, and 1.20). For each sub-group, four different plate's offsets were studied (S/d_b = 1.00, 1.50, 2.00 and 2.50). The total number of these studied specimens is 108.

The bars were embedded in concrete prisms with the same concrete cover for all specimens and equal to three bar's diameter to maintain the same conditions of Phase I. Five times of bar's diameter was the splice length for all studied specimens. The adopted notation system of specimens reveals the variety of studied parameters; where for specimen Fw-Dx-Ty-Sz; "w" indicates the concrete cylinder strength (25, 40, and 55), "x" refers to the bar diameter (12, 18, and 25), "y" is the plate thickness to bar's diameter ratio (0.40, 0.80 and 1.20) and "z" is the plate offset to bar's diameter ratio (1.00, 1.50, 2.00 and 2.50). For the lab-tested specimens, the back of the plates was covered by concrete with a thickness of three times the bar's diameter ($3d_b$), along this zone the bars were isolated by bond-breakers. However, the cover of the plate's back zone and sides for the specimens of parametric study is eliminated to keep the focus of the study on the bearing strength induced by the plates. Table 7 summarizes the suggested parameters and notation of all specimens.

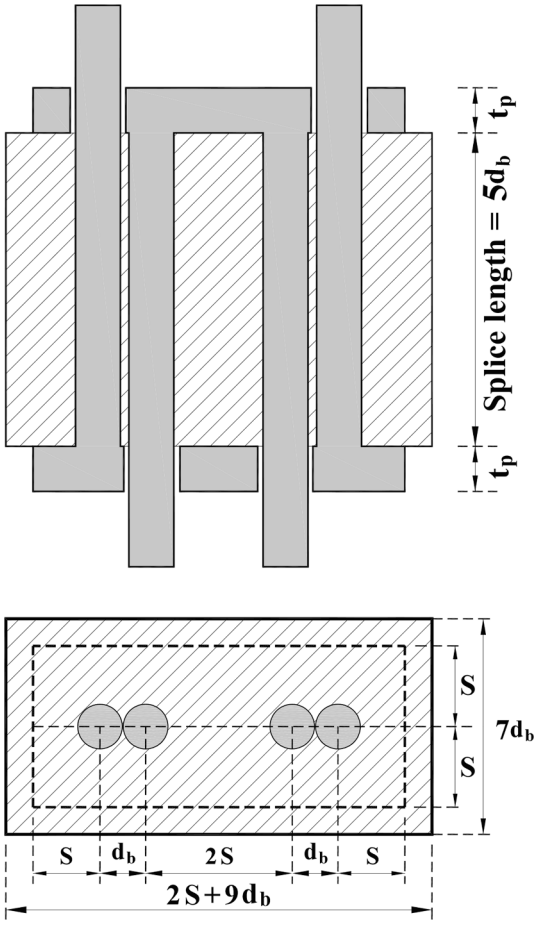


Fig. 28. Configuration of the anchor-ended specimens included in the parametric study.

3.5.1. Modeling of the suggested specimens

The previously mentioned constitutive material models were used to define the material characteristics of the studied specimens. The steel bars' yield/ultimate strengths were defined as 450/650 MPa for all specimens while, the concrete grades were defined as 25, 40, and 55 MPa. The characteristics of steel plates were based on the nominal yield/ultimate strengths namely 360/520 MPa. Solid element hexahedral 8-node element (C3D8R) was configured for both steel and concrete. The local bond-slip characteristics were defined according to the model code CEB-FIP (1990), where the maximum bond strength of 25, 40, and 55 MPa concrete grades are 5, 6.3, and 7.4 MPa, respectively, while the ultimate slip $S_1 = S_2 = 0.60$ mm with $S_3 = 2.50$ mm final slip. Subsequently, the cohesive behavior inputs K_{ss}/K_{tt} per unit area are equal to 8.3, 10.5, and 12.3 N/mm, respectively, and the fracture energies calculated for damage evolution are equal to 4.7, 6, and 7 N.mm, respectively.

The meshing and boundary conditions of a specimen of the parametric study are shown in Fig. 29. For specimens modeled for validation, the whole specimen was included in the modeling. For the suggested specimens of the parametric study, to reduce the consumed time for analysis, only half of the specimen was modeled to exploit the symmetrical geometry of specimens. On the plane of symmetry, the displacements have been restricted along X and Z directions while the rotations were also restricted about X and Y axes. At the bottom end of the lower steel bar, the displacement of this surface was restrained in all directions. The axial load was applied by imposing a smooth force function at the top end of the upper steel bar.

All of the suggested specimens were analyzed and the results were listed in terms of the ultimate load of specimens as well as the ratio between the ultimate loads of specimens and the maximum tensile strength as shown in Table 7. Two modes of failures were noticed, crushing of concrete between plates or rupture of reinforcing bars at a maximum tensile strength of the bars, as shown in Fig. 30. Fig. 30-a shows specimen F25-D12-T0.8-S2.0 that failed due to concrete crushing, the maximum principal plastic strain on the deformed shape indicates a plane at which the concrete elements exceeded the maximum tensile strain of concrete simultaneous with a sudden drop in the load applied to the steel bars. The plane of the tensile failure is caused by the axial compressive force between the two plates. Generally, based on the numerical analysis outputs, it was clear that the concrete grade, thickness (t_p), and offset (S) of the steel plates is directly affecting the capacity of the specimens.

3.5.2. Analysis of results

The ultimate capacities of the suggested specimens are summarized in Table 7. The output data of the modeled 108 suggested specimens were analyzed to investigate the relationship between the studied parameters and the specimen's capacity, in case of failure due to concrete crushing. The statistical analysis of the output data revealed an equation to estimate the capacity of the specimen.

Table 7
Parameters, notation, predicted and ultimate capacity of the modeled specimen.

Parameter			f_c'=25 MPa				f_c'=40 MPa					f_c'=55 MPa				
d_b	t_p/d_b	S/d_b	Specimen notation	Ult. load (kN)	Ult. load to max. strength	Predicted ult. load (kN)	predicted to Ult. loads	Specimen notation	Ult. load (kN)	Ult. load to max. strength	Predicted ult. load (kN)	predicted to Ult. loads	Specimen notation	Ult. load (kN)	Ult. load to max. strength	Predicted ult. load (kN)	predicted to Ult. loads
12 mm	0.40	1.00	F25-D12-T0.4-S1.0	27	0.184	15.3	0.57	F40-D12-T0.4-S1.0	35.2	0.24	24.5	0.70	F55-D12-T0.4-S1.0	49.5	0.337	33.7	0.68
		1.50	F25-D12-T0.4-S1.5	32	0.218	23.5	0.73	F40-D12-T0.4-S1.5	43.2	0.294	37.6	0.87	F55-D12-T0.4-S1.5	52.3	0.356	51.7	0.99
		2.00	F25-D12-T0.4-S2.0	34	0.231	32.5	0.96	F40-D12-T0.4-S2.0	47.5	0.323	52	1.09	F55-D12-T0.4-S2.0	66.5	0.453	71.5	1.08
		2.50	F25-D12-T0.4-S2.5	38	0.259	42.2	1.11	F40-D12-T0.4-S2.5	59.5	0.405	67.5	1.13	F55-D12-T0.4-S2.5	83.2	0.566	92.8	1.12
	0.80	1.00	F25-D12-T0.8-S1.0	46	0.313	50.3	1.09	F40-D12-T0.8-S1.0	69.2	0.471	80.4	1.16	F55-D12-T0.8-S1.0	92.1	0.627	110.6	1.20
		1.50	F25-D12-T0.8-S1.5	73	0.497	77.2	1.06	F40-D12-T0.8-S1.5	126.7	0.862	123.6	0.98	F55-D12-T0.8-S1.5	146.9	1	146.9	1.00
		2.00	F25-D12-T0.8-S2.0	108	0.735	106.8	0.99	F40-D12-T0.8-S2.0	146.9	1	146.9	1.00	F55-D12-T0.8-S2.0	146.9	1	146.9	1.00
		2.50	F25-D12-T0.8-S2.5	127	0.865	138.5	1.09	F40-D12-T0.8-S2.5	146.9	1	146.9	1.00	F55-D12-T0.8-S2.5	146.9	1	146.9	1.00
	1.20	1.00	F25-D12-T1.2-S1.0	50	0.34	50.3	1.01	F40-D12-T1.2-S1.0	77.8	0.53	80.4	1.03	F55-D12-T1.2-S1.0	112.2	0.764	110.6	0.99
		1.50	F25-D12-T1.2-S1.5	87	0.592	77.2	0.89	F40-D12-T1.2-S1.5	146.9	1	146.9	1.00	F55-D12-T1.2-S1.5	146.9	1	146.9	1.00
		2.00	F25-D12-T1.2-S2.0	132	0.899	106.8	0.81	F40-D12-T1.2-S2.0	146.9	1	146.9	1.00	F55-D12-T1.2-S2.0	146.9	1	146.9	1.00
		2.50	F25-D12-T1.2-S2.5	146.9	1	146.9	1.00	F40-D12-T1.2-S2.5	146.9	1	146.9	1.00	F55-D12-T1.2-S2.5	146.9	1	146.9	1.00
18 mm	0.40	1.00	F25-D18-T0.4-S1.0	57	0.173	34	0.60	F40-D18-T0.4-S1.0	78.58	0.238	54.4	0.69	F55-D18-T0.4-S1.0	103.2	0.313	74.8	0.72
		1.50	F25-D18-T0.4-S1.5	65	0.197	52.2	0.80	F40-D18-T0.4-S1.5	90.5	0.274	83.6	0.92	F55-D18-T0.4-S1.5	121.2	0.367	114.9	0.95
		2.00	F25-D18-T0.4-S2.0	73	0.221	72.2	0.99	F40-D18-T0.4-S2.0	110.3	0.334	115.6	1.05	F55-D18-T0.4-S2.0	152.2	0.461	158.9	1.04
		2.50	F25-D18-T0.4-S2.5	81	0.245	93.7	1.16	F40-D18-T0.4-S2.5	142.3	0.431	149.9	1.05	F55-D18-T0.4-S2.5	184.5	0.559	206.2	1.12
	0.80	1.00	F25-D18-T0.8-S1.0	99.5	0.301	111.7	1.12	F40-D18-T0.8-S1.0	166.7	0.505	178.8	1.07	F55-D18-T0.8-S1.0	202.7	0.614	245.8	1.21
		1.50	F25-D18-T0.8-S1.5	159	0.482	171.7	1.08	F40-D18-T0.8-S1.5	281.2	0.852	274.7	0.98	F55-D18-T0.8-S1.5	301.2	0.912	377.7	1.25
		2.00	F25-D18-T0.8-S2.0	237	0.718	237.3	1.00	F40-D18-T0.8-S2.0	330.2	1	330.2	1.00	F55-D18-T0.8-S2.0	330.2	1	330.2	1.00
		2.50	F25-D18-T0.8-S2.5	286	0.866	307.9	1.08	F40-D18-T0.8-S2.5	330.2	1	330.2	1.00	F55-D18-T0.8-S2.5	330.2	1	330.2	1.00
	1.20	1.00	F25-D18-T1.2-S1.0	107.5	0.326	111.7	1.04	F40-D18-T1.2-S1.0	184.8	0.56	178.8	0.97	F55-D18-T1.2-S1.0	258.5	0.783	245.8	0.95
		1.50	F25-D18-T1.2-S1.5	192.6	0.583	171.7	0.89	F40-D18-T1.2-S1.5	300.1	0.909	274.7	0.92	F55-D18-T1.2-S1.5	330.2	1	330.2	1.00
		2.00	F25-D18-T1.2-S2.0	300	0.909	237.3	0.79	F40-D18-T1.2-S2.0	330.2	1	330.2	1.00	F55-D18-T1.2-S2.0	330.2	1	330.2	1.00
		2.50	F25-D18-T1.2-S2.5	330.2	1	330.2	1.00	F40-D18-T1.2-S2.5	330.2	1	330.2	1.00	F55-D18-T1.2-S2.5	330.2	1	330.2	1.00
25 mm	0.40	1.00	F25-D25-T0.4-S1.0	106	0.166	64.9	0.61	F40-D25-T0.4-S1.0	143.1	0.224	103.9	0.73	F55-D25-T0.4-S1.0	182.7	0.286	142.9	0.78
		1.50	F25-D25-T0.4-S1.5	123	0.193	99.8	0.81	F40-D25-T0.4-S1.5	166.7	0.261	159.7	0.96	F55-D25-T0.4-S1.5	202.3	0.317	219.6	1.09
		2.00	F25-D25-T0.4-S2.0	143	0.224	138	0.97	F40-D25-T0.4-S2.0	190.2	0.298	220.7	1.16	F55-D25-T0.4-S2.0	259.5	0.407	303.5	1.17
		2.50	F25-D25-T0.4-S2.5	154	0.241	179	1.16	F40-D25-T0.4-S2.5	259.6	0.407	286.4	1.10	F55-D25-T0.4-S2.5	357.5	0.56	393.8	1.10
	0.80	1.00	F25-D25-T0.8-S1.0	185	0.29	213.4	1.15	F40-D25-T0.8-S1.0	307.5	0.482	341.4	1.11	F55-D25-T0.8-S1.0	397.8	0.623	469.5	1.18
		1.50	F25-D25-T0.8-S1.5	303	0.475	327.9	1.08	F40-D25-T0.8-S1.5	550.3	0.862	524.7	0.95	F55-D25-T0.8-S1.5	607.2	0.951	721.4	1.19
		2.00	F25-D25-T0.8-S2.0	435	0.681	453.3	1.04	F40-D25-T0.8-S2.0	638.3	1	638.3	1.00	F55-D25-T0.8-S2.0	638.3	1	638.3	1.00
		2.50	F25-D25-T0.8-S2.5	555	0.869	588.2	1.06	F40-D25-T0.8-S2.5	638.3	1	638.3	1.00	F55-D25-T0.8-S2.5	638.3	1	638.3	1.00
	1.20	1.00	F25-D25-T1.2-S1.0	200	0.313	213.4	1.07	F40-D25-T1.2-S1.0	341.4	0.535	341.4	1.00	F55-D25-T1.2-S1.0	498.7	0.781	469.5	0.94
		1.50	F25-D25-T1.2-S1.5	361	0.566	327.9	0.91	F40-D25-T1.2-S1.5	578.1	0.906	524.7	0.91	F55-D25-T1.2-S1.5	638.3	1	638.3	1.00
		2.00	F25-D25-T1.2-S2.0	576	0.902	453.3	0.79	F40-D25-T1.2-S2.0	638.3	1	638.3	1.00	F55-D25-T1.2-S2.0	638.3	1	638.3	1.00
		2.50	F25-D25-T1.2-S2.5	638.3	1	638.3	1.00	F40-D25-T1.2-S2.5	638.3	1	638.3	1.00	F55-D25-T1.2-S2.5	638.3	1	638.3	1.00

Ult. Load = the ultimate load obtained by ABAQUS, Ult. load to max. strength = the ultimate load obtained by ABAQUS divided by the ultimate tensile force of the bars, Predicted ult. load = the ultimate load estimated by the proposed equation, Predicted to ult. load = the ultimate load estimated by the proposed equation divided by the ultimate load obtained by ABAQUS.

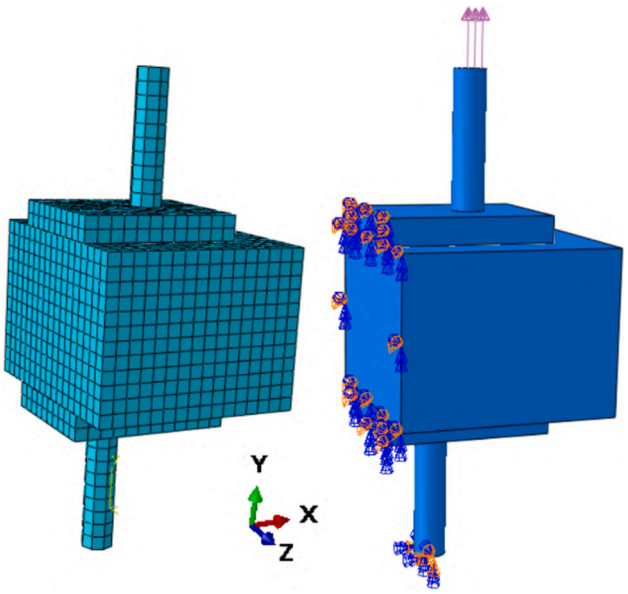


Fig. 29. Boundary conditions and meshing of a plate-ended specimen included in the parametric study.

3.5.2.1. Effect of concrete strength. Since crushing concrete is the governing mode of failure for most of the studied specimens, the concrete grade is one of the most effective parameters. Regardless of the concrete grade, all specimens with thickness ratio t_p/d_b = 0.40 failed due to concrete crushing. Subsequently, to investigate the influence of concrete grade on the capacity of the specimens failed by concrete crushing, the ultimate load to the ultimate tensile strength ratio is plotted against the concrete grade for specimens of sub-group of thickness ratio t_p/d_b = 0.40 as shown in Fig. 31.

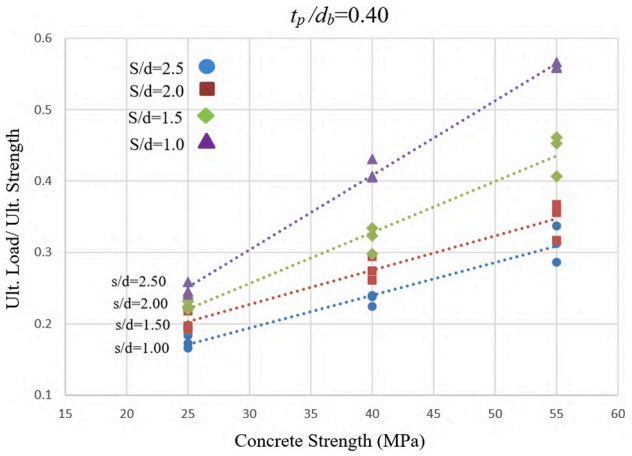
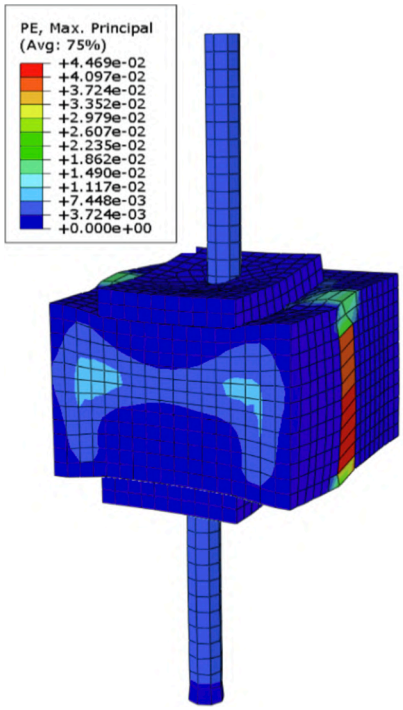
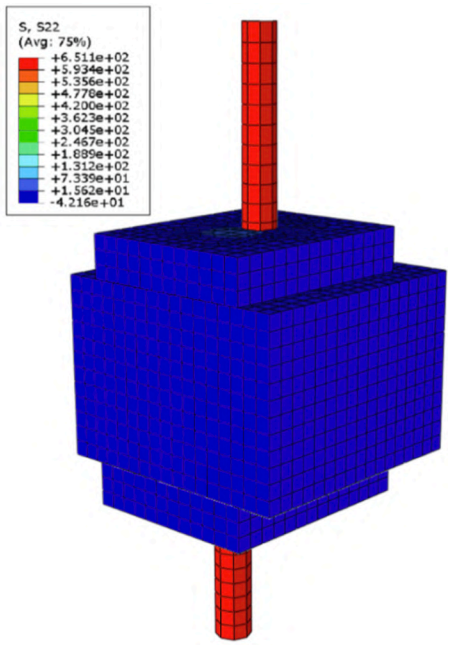


Fig. 31. Ultimate load/ultimate strength ratio vs the concrete grade (t_p/d_b = 0.40).

The specimens were classified among the sub-group of thickness ratio of 0.40 by the ratio of plate offset S/d_b. The capacity of all specimens with the same S/d_b ratio of sub-group thickness ratio 0.40 was linearly proportional to the concrete grade as shown in Fig. 31. However, the other sub-groups of thickness ratio 0.80 and 1.20 showed the linear behavior only at the lowest ratio S/d_b = 1.0. This is attributed to the dissimilar mode of failure. Many specimens with a high S/d_b ratio have a larger area, subsequently, a higher bearing capacity for plates is



(a) Maximum principal plastic strain of F25-D12-T0.8-S2.0 shows concrete crushing between plates.



(b) Bar's tensile stress of F25-D12-T1.2-S2.5 shows maximum tensile strength of steel.

Fig. 30. Modes of failure exhibited by the suggested specimens.

gained, thus their failure is due to the rapture of bars and their maximum capacity is not caused by the crushing of concrete. Eventually, the maximum force (*F*) attained by all specimens that failed due to concrete crushing is linearly proportional to the concrete grade.

$$F\ \alpha\ f_c^{'} \tag{2}$$

where F = the maximum splice strength failed due to concrete crushing; α refers to the proportionality symbol.

3.5.2.2. Effect of plate's offset ratio. The plate offset affects the stiffness of the plate as well as the compressed area, it affects the quantity and the distribution of the compression stress under the plate. To investigate the influence of the plate's offset ratio on the capacity of the specimens, the ultimate load to ultimate strength ratio is plotted against the plate's area for the sub-group of thickness ratio 0.40 at which all specimens failed due to concrete crushing between the plates. Specimens with a bar diameter of 18 mm with a sub-group of $t_p/d_b = 0.40$ were selected to show the relationship, the plot is shown in Fig. 32. Taking into consideration that the plate's area shows the same response also with specimens of 12 and 25 mm bars. For the lowest thickness ratio (t_p/d_b = 0.40), regardless of concrete grade, it is obvious that the specimen's capacity is linearly proportional to the plate's area. However, for other sub-groups of thickness ratios 0.8 and 1.20, the capacity of specimens with concrete grade 25 MPa only was linearly proportional to the plate's area. Many specimens with a higher thickness ratio (t_p/d_b = 0.80 and 1.20) have a higher stiffness. Subsequently, a better distribution of compression stress is attained then a higher bearing capacity for plates is reached. Therefore, their failure is due to the rapture of bars and their maximum bearing capacity is out of scope. Eventually, the maximum force (*F*) attained by all specimens that failed due to concrete crushing is linearly proportional to the area of the plates.

$$F\ \alpha\ S\,(2S + d_b) \tag{3}$$

3.5.2.3. Effect of plate's thickness ratio. From the previously illustrated analysis of the effective parameters, the relationship between the ultimate load (F) and both of plate's area and concrete grade is linear. On the other hand, the effect of plate thickness is not clear yet. To estimate the relationship between the ultimate load and the plate's thickness, all specimens with concrete grade 25 MPa were selected and the reason is that the majority of these specimens failed due to the crushing of concrete. The relationship between the load ratio/offset ratio against the thickness ratio is plotted as shown in Fig. 33. Using the regression analysis, the equation that represents this relationship is estimated as follows:

$$\frac{F}{F_u \times (s/d_b)} = 1.04\,(\frac{t_p}{d_b}) - 0.44\,(\frac{t_p}{d_b})^2 - 0.21 \tag{4}$$

Note that, $R^2 = 0.92$ which means a strong quadratic relationship.

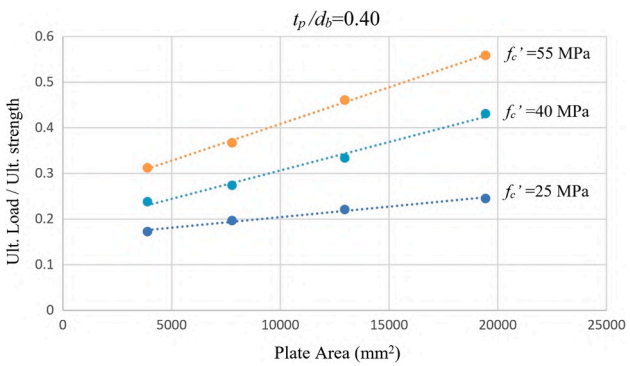


Fig. 32. Ultimate load/ultimate strength ratio vs the plate's area for 18 mm bars and $t_p/d_b = 0.40$.

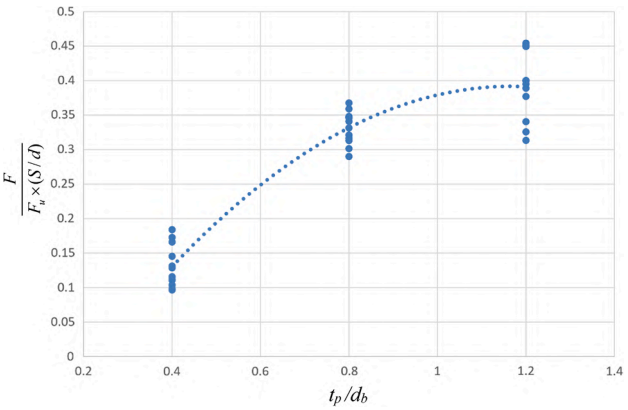


Fig. 33. Load ratio/offset ratio vs the thickness ratio relationship.

3.5.3. Proposed equation to predict the capacity of plate-ended specimens

By combining all parameters in a single equation and then eliminating the redundant terms, the final formulation including all parameters could be expressed by the following:

$$F\ \alpha f_c^{'}\ \times (\frac{S}{d_b}) \times S \times (2S + d_b)\ \left[\ 4t_p d_b - 2t_p^2 - d_b^2\right] \tag{5}$$

To find the constants that make this equation applicable, the Solver tool of the commercial known software "Excel" was used to perform a multiple linear regression analysis. It was also found that the predicted loads show better values if the terns of "S" and "d" in the fraction (S/d) are raised to powers. The statistically assumed constants (a_1, a_2, a_3) are as follows:

$$F\ = a_1 \times f_c^{'}\ \times (\frac{S^{a2}}{d_b^{a3}}) \times (2S + d_b)\ \left[4t_p d_b - 2t_p^2 - d_b^2\right] \leqslant F_u \tag{6}$$

After performing the analysis on all 108 suggested specimens with the previously illustrated parameters, the best values of the constants (a_1, a_2, a_3) are 5.45, 0.35, and 1.38, respectively, and the final equation becomes as follows:

$$F\ = 5.45 \times f_c^{'}\ \times (\frac{S^{0.35}}{d_b^{1.38}}) \times (2S + d_b)\ \left[4t_p d_b - 2t_p^2 - d_b^2\right] \leqslant F_u \tag{7}$$

Note that, all units are in N and mm. The predicted ultimate loads via this proposed equation are listed in Table 7. By using this equation to predict the ultimate load achieved by the suggested specimens, statistical analysis for the ratio between the predicted to numerically conducted ultimate loads revealed a mean value = 0.988 and a coefficient of variance = 0.134. The relationship between the predicted/ultimate loads vs the offset ratio of the plate was plotted as shown in Fig. 34.

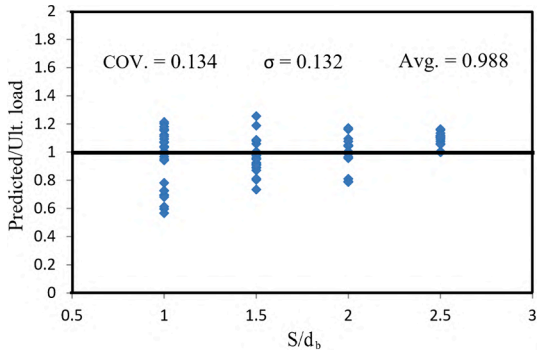


Fig. 34. Predicted/ultimate load vs the offset ratio of the plates.

4. Conclusion

The research aimed to evaluate the adequacy of the developed technique used to enhance the performance of conventional lap splices. Two phases of the experimental tests were carried out, Phase I studied splices in HPC prisms without confining reinforcement subjected to axial tension, while Phase II assessed the flexural behavior of large-scale RC beams that contained the same splices under the same conditions. Two sub-groups were studied in each phase, straight-ended and anchor-ended spliced bars. Based on the experimental findings of the current study as well as the numerical parametric study, the following conclusions can be outlined.

1. The failure of the plate-ended beams was characterized by suppressing tension cracks within the splice zone between the plates until failure; this may be attributed to the slip-induced moving plates that converted the tensile force of bars into compression force acting between the plates.
2. The plate-ended is an advantageous technique as it can avoid the local failure that might be caused by stress localization of the conventional headed bars by enlargement of the anchoring area. In addition, the tensile cracks within the splice zone played a role in accelerating the bond failure of straight-ended splices, however, restricting these cracks in plate-ended splices contributed to strengthening the splice.
3. The rupture of reinforcing bars at the maximum tensile strength was attained by all plate-ended specimens of Phase I owing to the bearing capacity gained by the anchoring plates.
4. Splices of lengths 5 and $10d_b$ of plate-ended specimens of Phase I remained without noticeable tensile cracks until failure owing to the effect of the plates which transformed the tensile force of bars into compression force acting between plates.
5. Specimens having a splice length of $20d_b$ succeeded to achieve their design force in both of the experimental phases, however, B-O-20d failed to overcome all cyclic loading stages and exhibited low energy dissipation and low maximum deflection compared to those of the control beam W–D.
6. The beams of straight-ended splices with 5, 10, 20, and $30d_b$ of splice length failed at 42.8, 63.7, 90.1, and 100.2 %, respectively; of the corresponding maximum load attained by the control beam W–D.
7. The beams of straight-ended splices with 5, 10, 20, and $30d_b$ of splice length failed at 6.4, 11.2, 17.5, and 95.2 %, respectively; of the corresponding maximum deflection exhibited by the control beam W–D.
8. For straight-ended bars of the current research, it was found that the minimum splice length to achieve the bars' design force in addition to providing reasonable ductile performance is 30 d_b.
9. For beams of Phase II, the newly developed technique of plate-ended splice showed high energy dissipation as well as maximum deflection compared to those of the control beam. The plate-ended splice of $5d_b$ length was found to be enough to overtake the yielding of tension steel bars in addition to showing the same ductility performance of the control beam W–D.
10. Based on a statistical analysis of the findings of 108 suggested plate-ended specimens modeled using FEM, a proposed equation was established to predict the ultimate strength of anchor-ended splices.

In the current experimental program, all anchor-ended specimens/beams of Phase I and II failed away from the splice after reaching the maximum tensile strength of the steel reinforcing bars, thus, the effect of the plate's dimensions was not clear in the experimental study and it had a further assessment in the numerical study. The conducted equation to design the anchoring plates is limited to this study and still needs a future extension including a wide experimental program studying the effect of the concrete strength and the plate's dimensions. It is worth mentioning that the newly developed plate-ended technique also needs further studies having several configurations that allow it to anchor multiple bars.

Data availability.

The raw data required to reproduce these findings are available only with direct contact through email to the corresponding author.

Declaration of Competing Interest

The authors declare that they have no known competing financial interests or personal relationships that could have appeared to influence the work reported in this paper.

Data availability

Data will be made available on request.

References

[1] Tepfers R. A theory of bond applied to overlapped tensile reinforcement splices for deformed bars. Division of concrete structures 1973: 328 pp. Chalmers University of Technology, Goteborg, Sweden.
[2] Orangun O, Jirsa O, Breen E. Reevaluation of test data on development length and splices. ACI Journal 1977;74(3):114–22.
[3] Darwin D, McCabe L, Idun K, Schoenekase P. Development length criteria: bars not confined by transverse reinforcement. ACI Struct J 1992;89(6):709–20.
[4] Esfahani R, Vijaya V. Local bond strength of reinforcing bars in normal strength and high-strength concrete (HSC). ACI Struct J 1998;95(2):96–106.
[5] Esfahani R, Vijaya V. Bond between normal strength and high-strength concrete (HSC) and reinforcing bars in splices in beams. ACI Struct J 1998;95(3):272–80.
[6] Azizinamini A, Stark M, Roller J, Ghosh K. Bond performance of reinforcing bars embedded in high-strength concrete. ACI Struct J 1993;90(5):554–61.
[7] Azizinamini A, Chisala M, Ghosh K. Tension development length of reinforcing bars embedded in high-strength concrete. Eng Struct 1995;17(7):512–22.
[8] Aire C, Mendoza C, Davila P. Polypropylene fibers reinforced concrete: optimization on plastic shrinkage cracking. Proceedings of the Second International Conference on Future Concrete. 2011.
[9] Zhang P, Li Q. Effect of polypropylene fiber on durability of concrete composite containing fly ash and silica fume. Compos B 2013;45:1587–94.
[10] Saje D, Bandelj B, Šušteršič J, Lopatič J, Saje F. Shrinkage of polypropylene fibre reinforced high performance concrete. J Mater Civ Eng 2011;23(7):941–95.
[11] Marchand P, Baby F, Khadour A, Battesti T, Rivillon P, Quiertant M, et al. Bond behavior of reinforcing bars in UHPFRC. Mater Struct 2016;49:1979–95.
[12] Choi W, Jang S, Yun H. Bond and cracking behavior of lap-spliced reinforcing bars embedded in hybrid fiber reinforced strain-hardening cementitious composite (SHCC). Compos B 2017;108:35–44.
[13] Metelli G, Marchina E, Plizzari GA. Experimental study on staggered lapped bars in fiber reinforced concrete beams. Compos Struct 2017;179:655–64.
[14] Eligehausen R. Bond in Tensile Lapped Splices of Ribbed Bars with Straight Anchorages. Publication 301, German Institute for Reinforced Concrete, Berlin 1979.
[15] Darwin D, Tholen M, Idun E, Zuo J. Splice strength of high relative rib area reinforcing bars. ACI Struct J 1996;93(1):95–107.
[16] Joint ACI-ASCE Committee 408. Bond and Development of Straight Reinforcing Bars in Tension (ACI 408R-03). American Concrete Institute, Farmington Hills, MI, 2003, 49 pp.
[17] Darwin D, Graham K. Effect of deformation height and spacing on bond strength of reinforcing bars. ACI Struct J 1993;90(6):646–57.
[18] Darwin D, Graham K. Effect of Deformation Height and Spacing on Bond Strength of Reinforcing Bars. SL Report 93-1, University of Kansas Center for Research, Lawrence, Kans., 1993b.
[19] Issa CA, Nasr A. An experimental study of welded splices of reinforcing bars. Build Environ 2006;41:1394–405.
[20] Vella JP, Vollum RL, Jackson A. Investigation of headed bar joints between precast concrete panels. Eng Struct 2017;138:351–66.
[21] Fawzy T, Khalil A-H, Atta A, Afefy HM,| Ellithy M. Experimental and analytical study on tension lap splices in nonconventional concrete using different techniques. Structural Concrete 2020; 1 – 15.
[22] S. Abed H, Abed J, Al-Rawe H. Anchorage behavior of headed bars in reinforced concrete beams. Struct 2021;29:1954–1959.
[23] Kim K, Park K, Park C. Structural behavior of expanded rib steel bars used in reinforced concrete beams. Resul Eng 2022;14:100455.
[24] Burkhardt C. Behavior of lap splices in high strength concrete. Ph.D thesis, Aachen, Germany: RWTH Aachen University; 2000; p. 190 [in German].
[25] Richter B. A new perspective on the tensile strength of lap splices in reinforced concrete members. M.Sc thesis, West Lafayette, USA Purdue University; 2012. p. 165.
[26] Lagier F, Massicotte B, Charron J. Bond strength of tension lap splice specimens in UHPFRC. Constr Build Mater 2015;93:84–94.

[27] ASTM, 2010. Standard test methods and definitions for mechanical testing of steel products – Annex A9 methods for testing steel reinforcing bars. A370. ASTM West Conshohocken, PA, USA.
[28] Horszczaruk EK. Hydro-abrasive erosion of high performance fiber-reinforced concrete. Wear 2009;267:110–5.
[29] ASTM. Standard test method: compressive strength of Cylindrical Concrete Specimens, C39/C39M. ASTM West Conshohocken, PA, USA; 2010.
[30] Hwang H, Park H, Yi W. Nonuniform bond stress distribution model for evaluation of bar development length. ACI Struct J 2017;114(4):839–49.
[31] Lin H, Zhao Y, Ozbolt J, Feng P, Jiang C, Eligehausen R. Analytical model for the bond stress-slip relationship of deformed barsin normal strength concrete. Constr Build Mater 2019;198:570–86.
[32] Jacques E, Saatcioglub M. Bond-slip modelling of reinforced concrete lap splices subjected to low and high strain rates. Eng Struct 2019;195:568–78.
[33] ABAQUS. Abaqus/CAE User's Manual. Dassault Systemes Simulia Corp, Providence; RI: USA.
[34] Saenz LP. Discussion of "Equation for the stress-strain curve of concrete" by Desayi P, Krishnan S". ACI J 1964;61:1229–35.
[35] Hu H, Schnobrich W. Constitutive modelling of concrete by using non associated plasticity. J Mater Civ Eng (ASCE) 1989;1:199–216.
[36] Wollrab E, Kulkarni SM, Ouyang C, Shah SP. Response of reinforced concrete panels under uniaxial tension. ACI Struct J 1996;93(6):648–57.
[37] ACI Committee 318. Building Code Requirements for Structural Concrete (ACI 318-19) and Commentary (ACI 318R-18). American Concrete Institute, Farmington Hills, MI, 2019.
[38] Hadjazi K, Sereir Z, Amziane S. Cohesive zone model for the prediction of interfacial shear stresses in a composite plate RC beam with an intermediate flexural crack. Compos Struct 2012;94:3574–82.
[39] Sakr MA, El-khoriby SR, Khalifa TM, Nagib MT. Modeling of RC shear walls strengthened by FRP composites. Struct Eng Mech 2017;61:407–17.
[40] CEB-FIP. Comité Euro-International du Béton (Model Code 1990). Lausane, France; 1990.